CHEMICAL REVIEWS

Volume 109, Number 5

Electron Tomography for Heterogeneous Catalysts and Related Nanostructured Materials

Heiner Friedrich,*,† Petra E. de Jongh,† Arie J. Verkleij,‡ and Krijn P. de Jong*,†

Inorganic Chemistry and Catalysis, Debye Institute for Nanomaterials Science, Utrecht University, Sorbonnelaan 16, 3584 CA, Utrecht, The Netherlands, and Molecular Cell Biology, Utrecht University, Padualaan 8, 2584 CH, Utrecht, The Netherlands

Received October 15, 2008

Contents

1. Introduction

The full potential in catalyst development will only be realized if characterization techniques are available that can probe materials with subnanometer resolution. One of the most employed techniques to image heterogeneous catalysts at the nanometer and subnanometer scale is transmission electron microscopy (TEM). As suggested by the name, TEM uses electrons transmitted through the object for imaging. Since the interaction between electrons and matter is very strong, only thin parts, commonly much less than a micron in thickness, are imaged. Since heterogeneous catalysts are, in most cases, structured on a much smaller length scale, the sample thickness can be reduced to TEM requirements by appropriate preparation techniques and is, therefore, no limitation.

* Corresponding author. E-mail: h.friedrich@uu.nl and k.p.dejong@uu.nl. Phone: +31 30 253 7400. Fax: +31 30 251 1027.
† Inorganic Chemistry and Catalysis, Debye Institute for Nanomaterials Science, Utrecht University.
‡ Molecular Cell Biology, Utrecht University.

The major advantage of electron microscopy is that a variety of modes to probe the sample can be employed, of which conventional TEM (TEM), diffraction mode, scanning TEM (STEM), and spatially resolved elemental analysis are only a few examples. For a detailed description of available TEM techniques, we refer to the books by Williams and Carter,[1] Reimer,[2] and Yao and Wang.[3] Focusing on the use of electron microscopy in heterogeneous catalysis, the book by Gai and Boyes[4] provides a wealth of information. Shorter reviews focusing on catalysis-related applications of TEM,[5−10] environmental TEM,[11] and electron energy-loss spectroscopy[12] are also available.

The principal beam paths for imaging in TEM and STEM mode are sketched in Figure 1. In TEM, the sample is probed by a parallel electron beam, resulting in a bright-field image. Electrons that are scattered onto the contrast-forming objective aperture blade are removed from the beam and will not be recorded in the image. Thus, thick objects and objects of high mass-density will appear dark in such an image (scattering or absorption contrast). In STEM, a focused electron beam is rastered across the sample. The electrons recorded at each point of the raster then form the image. When a ring detector (annular dark-field detector) is used to collect deflected electrons, thick objects and objects of high mass-density will appear bright in such images. This scheme explains the most basic connection between contrast in an image and the imaged structure. Other sources of contrast, which may dominate depending on the nature of the specimen, include diffraction contrast (associated with the orientation of a crystalline specimen with respect to the electron beam) and TEM phase contrast (tunable by defocusing). When going from nanometer resolution to atomic details, only accurate control of beam condition, sample orientation, and defocus setting yields interpretable results.

The above paragraph already hints toward one of the difficulties when interpreting TEM and STEM images. Since images are a two-dimensional (2D) representation of an originally three-dimensional (3D) structure, it is hard to distinguish between thick objects and objects of high mass-

10.1021/cr800434t CCC: $71.50
Published on Web 03/20/2009

Heiner Friedrich received his M.Sc. (2001) in Physics from the University of Dresden, working in the field of electron optics at the Triebenberg Laboratory for High-Resolution Electron Microscopy and Holography. Between 2002 and 2005, he joined Arizona State University (U.S.A.) as a research scientist to implement and apply electron tomography at the John M. Cowley Center for High-Resolution Electron Microscopy. Since 2005, his research, under the supervision of Prof. K. P. de Jong, Prof. A. J. Verkleij, and Dr. P. E. de Jongh, has focused on the quantitative three-dimensional characterization of nanostructured materials by electron tomography. His current interests include image analysis and structure modeling.

Petra E. de Jongh obtained her Ph.D. (Hons) in Physical Chemistry in 1999 from Utrecht University (The Netherlands). She then worked as a senior scientist at Philips Electronics on functional thin films for applications in batteries, thermochromic materials, and magnetic, optic, and electrical fingerprint coatings, resulting in about 10 patents. In 2004, she joined the Department of Inorganic Chemistry and Catalysis at Utrecht University as an assistant Professor. Her main interest is using advanced techniques to prepare and characterize nanostructured inorganic materials (typically nanoparticles in mesoporous supports) and gain insight into the impact of particle size, confinement, and pore structure on the functionality of these materials for applications in catalysis and hydrogen storage.

density (e.g., metals). Nevertheless, in some cases it is possible to extract sample thickness or chemical information.[12] This should not distract from the fact that the resolution in the third dimension is usually not better than the thickness of the sample, which might be several hundred nanometers. Thus, from a single image, the position of a metal particle with respect to its support, e.g., on the surface or in the inside, can only be inferred in rare cases. To overcome the issue, two or more images[13−15] or serial sectioning of the sample by microtomy[16] have been applied. Recent developments in optical sectioning by aberration-corrected STEM, which is, in a way, similar to confocal optical microscopy, hold great promise for the future.[17] For samples with a periodic architecture, electron crystallography can elucidate the 3D structure accurately.[5,7,18,19]

Arie J. Verkleij obtained his M.Sc. (1970) and Ph.D. (1975) in biology from the University of Utrecht. Since then he has occupied different positions: 1975−1985, Assistant Professor at the Institute of Molecular Biology University of Utrecht; from 1986 onwards, Professor in Cell Biology and Electron Microscopy, University of Utrecht; 1988−1993, President of the Dutch Society for Electron Microscopy; 1991−2004, Scientific Director of the Institute for Biomembranes, University of Utrecht; 2004 onwards, vice-dean Life Sciences, Faculty of Science, University of Utrecht. His current research interests include (i) signal transduction and cell cycle regulation, (ii) ischaemia and reactive oxygen species, and (iii) innovative solutions for structure analysis based on light and electron microscopy. He has published more than 300 scientific papers.

Krijn P. de Jong (1954) obtained his B.Sc. (1976), M.Sc. (1978), and Ph.D. (1982) degrees in chemistry, all degrees cum laude and at Utrecht University. In 1987, he also obtained an M.Sc. degree in chemical engineering from Twente University. From 1982−1997, he was with Shell Research working on catalyst preparation, heavy oil conversion, environmental processes, zeolite catalysis, and synthesis gas production and conversion. In 1997, he was appointed as full professor of inorganic chemistry and catalysis at Utrecht University. His current research interests are catalyst preparation, nanostructured catalysts, hydrocarbon conversions over zeolites, catalysts for fine chemicals manufacture, conversion of synthesis gas, and hydrogen storage. He has published about 120 scientific papers and more than 20 patents.

A general approach to 3D imaging of complex materials with a nonperiodic 3D structure is provided by electron tomography (ET). The growing importance of ET has been previously reviewed with emphasis on materials science[20,21] and biological sciences,[22−25] as well as in context with other nanotomographic techniques.[26,27] This review presents, after introducing the technical aspects of ET, a comprehensive overview to the rapidly emerging field of ET for the study of heterogeneous catalysts and related nanostructured materials. Sections are organized following the materials classes of zeolites, ordered mesoporous materials, disordered oxide supported catalysts, carbon materials, and miscellaneous materials (ceramics, polymers, and nanocomposites).

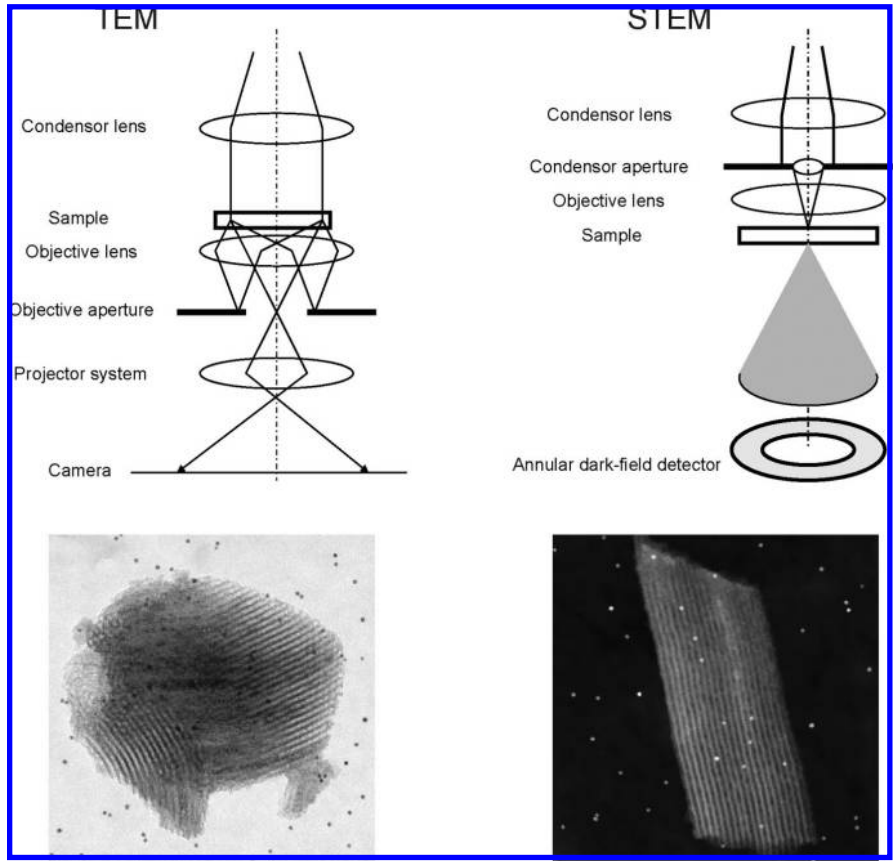

Figure 1. Schematic beam path in TEM and STEM. The images below, acquired in the corresponding imaging mode, show SBA-15 particles on a carbon support film with 5 nm gold spheres attached.

2. Technical Aspects

In ET, a series of 2D images (commonly 50−150 images) is collected by tilting the specimen in the electron beam and recording an image at each tilt step. Subsequently, the series of images (tilt series) is aligned with respect to a common origin and tilt axis. Finally, the 3D morphology of the object is reconstructed using numerical algorithms. Details of the workflow, from data acquisition to visualization of results, are given in section 2.3.

2.1. Basic Principle

The mathematical framework underlying tomography was developed by Johan Radon and forms the basis for what has come to be known as the Radon transform.[28] It applies to many situations where it is practicable to determine structural properties of an object from data that leave the object complete, e.g., by using transmitted waves or particles.[29] Applications range from X-ray tomography[30,31] to electron tomography in catalysis.[32,33] The Radon transform maps a real space object by its projections, which is equivalent to probing of a sample by a transmitted signal such as an electron beam. From these projections, the object structure can be reconstructed by applying the inverse Radon transform. To which extent TEM and STEM images can be considered to be projections will be discussed in section 2.4.

For a more intuitive understanding, a connection between the information in a series of projections and the 3D object structure is needed. To highlight this connection, we make use of the close relationship between the probably better known Fourier transform and the Radon transform. It can be shown that the Fourier transform of a 2D projection is equal to a central slice through the 3D Fourier transform of the object. For a detailed discussion of this theorem, the Projection-Slice theorem, we refer to the book by Deans.[29] A schematic representation of the tomographic reconstruction using the Projection-Slice theorem is depicted in Figure 2. By combining multiple projections, i.e., multiple central slices at different tilts, the 3D Fourier space of the object is sampled, and an inverse Fourier transform reconstructs the 3D object.

First strides toward tomography using electron micrographs date back to 1968.[34−36] Historically, the application of ET has been the domain of biology, where it is used to image the 3D structure from molecules to entire cells.[22−24] In the past decade, the range of materials studied by ET has extended dramatically. Enabling factors include the availability of large-area charge-coupled device (CCD) cameras and microscope automation.[37] Nowadays, a number of academic and commercial tools for automated data acquisition exist, such as UCSF tomography,[38] SerialEM,[39] TOM software toolbox,[40] EMMenu (TVIPS GmbH, Gauting, Germany), Xplore3D (FEI company, Eindhoven, The Netherlands), TEMography (JEOL Ltd., Tokyo, Japan), and Digital Micrograph 3D ET (Gatan Inc., Pleasanton, CA).

With the increasing diversity of samples examined by ET, imaging modes other than bright-field TEM gain importance. Which mode to choose, e.g., TEM versus STEM, will depend upon the combination of material and scientific questions. A comprehensive list of imaging modes that have been used for tomographic reconstruction is given in section 2.3. At present, mainly bright-field (BF) TEM tomography and high-angle annular dark-field (HAADF) STEM tomography are applied for studying catalysis-related nanostructured materials.

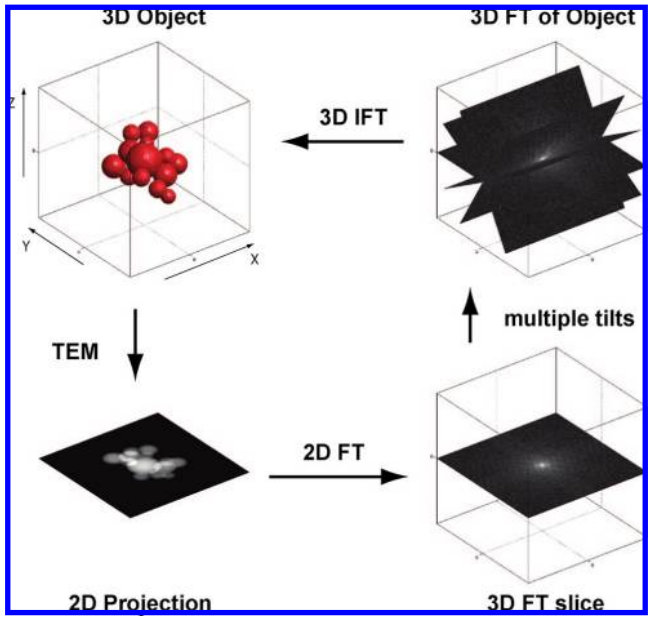

Figure 2. ET reconstruction scheme using the Projection-Slice theorem. FT denotes the Fourier transform, and IFT denotes the inverse Fourier transform. By combining projections recorded at multiple tilts (here shown for single-axis tilting around X), the 3D FT of the object is probed. An inverse Fourier transform then reconstructs the 3D object.

2.2. Resolution

In principle, electron tomograms can be reconstructed from any set of projections taken along different directions. However, mechanical and technical constraints prevent accurate and reproducible sample movement with six degrees of freedom, thus limiting the variety of practicable data-acquisition schemes. At this point, it has to be noted that the applied data-acquisition scheme largely determines the obtainable resolution. Here, we will restrict the discussion to single-axis tilting, although alternative approaches, such as conical tilting[41] and dual-axis tilting,[42,43] are also employed.

In single-axis tilting, the object is tilted in increments about the rotation axis of the microscope goniometer from one extreme of the tilt range to the other, e.g., from −70° to +70°. Assuming a perfect alignment, the resolution along the rotation axis (*x*-axis in Figure 2) is equal to the resolution in the original micrographs. The resolution in the direction perpendicular to the holder and beam axis (*y*-axis in Figure 2) is determined by the number of projections, *N*, and the diameter, *D*, of the reconstructed volume:[44]

$$d_y = \frac{\pi D}{N} \tag{1}$$

The above expression, referred to as Crowther criterion, assumes that the images are acquired over a range of ±90°. The resolution parallel to the beam direction (*z*-axis in Figure 2) is further affected as a result of the limited tilt range of the microscope goniometer or shadowing of the imaged area by the sample holder at high tilt angles. Angular limitations lead to a "missing wedge" of information that causes an elongation (e_{yz}) of the reconstruction point-spread function. The elongation factor can be estimated[45] from the maximum tilt angle (α) as follows:

$$d_z = d_y \cdot e_{yz} = d_y \cdot \sqrt{\frac{\alpha + \sin\alpha\cos\alpha}{\alpha - \sin\alpha\cos\alpha}} \tag{2}$$

On the basis of the above equations and Figure 2, it becomes clear that increasing the tilt range while decreasing the tilt increment will improve the resolution. A graphical representation of the effect of tilt increment and maximum tilt angle on reconstruction results is given in Figure 3. In practice, resolutions better than predicted by the Crowther criterion have been obtained but not understood.[20,46−49]

Alternatively to geometrical considerations as brought forward in the Crowther criterion, progress is made by defining standards for resolution estimation.[50−52] Unfortunately, a straightforward quantitative verification of resolution is not available for electron tomography.[25]

2.3. Workflow

First, a few comments about sample holders and sample preparation are necessary. As a result of the high tilts required for ET, typically ±70°, a high-tilt sample holder and a suitably prepared sample have to be used. The high-tilt sample holder allows for tilting of the specimen in the microscope to high angles without touching the objective lens pole piece or the objective aperture blade. Its construction also prevents shadowing of the viewable grid area by the holder edges. Single-tilt and tilt-rotate holders are commercially available.

The specimen grid should be chosen such that shadowing of the viewable area by the grid bars is minimal. In general, large-mesh grids or parallel-bar grids are best suited. In the first step, colloidal gold particles of 5−15 nm size, depending on the desired magnification, are deposited onto the TEM grid. The gold particles serve as markers and aid in the alignment of the tilt series. Gold markers are not mandatory but have proven to be a successful and straightforward approach.[53] In the second step, the sample material is placed on the (carbon) support film in form of a fine powder or an ultramicrotome section. Powders are commonly applied by ethanol suspension in an ultrasonic bath, subsequent application of a droplet of the suspension onto the grid, and then drying. For ET samples, dilute suspensions are favorable since a lower density of particles on the support film prevents shadowing by neighboring structures at high tilts. For microtome sections, tilting to high angles causes the effective beam path through the sample to increase. One should keep in mind while cutting the sections that the effective path length at 70° tilt is ∼3 times the section thickness.

Once the sample is ready, further steps and parameters from tilt-series acquisition to visualization of the final results are outlined in Figure 4. Acquisition is aided by automated corrections for specimen drift and focus during tilting.[38−40,54] As discussed in section 2.2, increasing the tilt range while decreasing the tilt increment will improve results. For acquisition of the tilt series, three main parameters are important: tilt range (∼±70° or higher), tilt increments (∼1−3°), and electron dose, commonly controlled by the image-acquisition time (∼1−4 s in TEM and 10−80 s in STEM). Since beam settings (e.g., spot size, condenser aperture, etc.) may differ significantly between TEM and STEM, a comparison of applied electron doses based on the acquisition times alone is inappropriate. In fact, one has to calculate for the given settings the total number of electrons imparted on the sample per unit area throughout tilt-series acquisition.

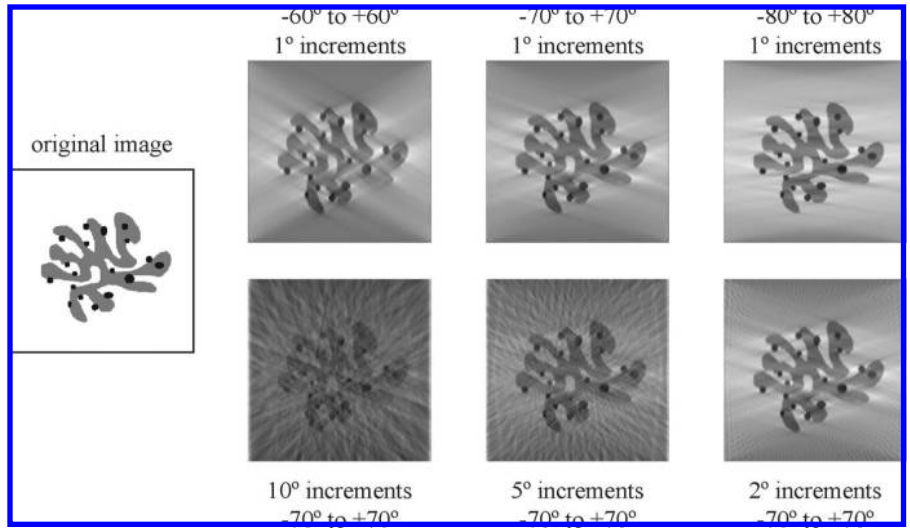

Figure 3. Effects of maximum tilt angle and tilt increment on the tomographic reconstruction. In general, increasing the maximum tilt angle and decreasing the tilt increment improves results. Bright zones to the left and right of dark objects result from the reconstruction point spread function (weighted backprojection), and dark zones on the bottom and top are caused by the limited maximum tilt angle.

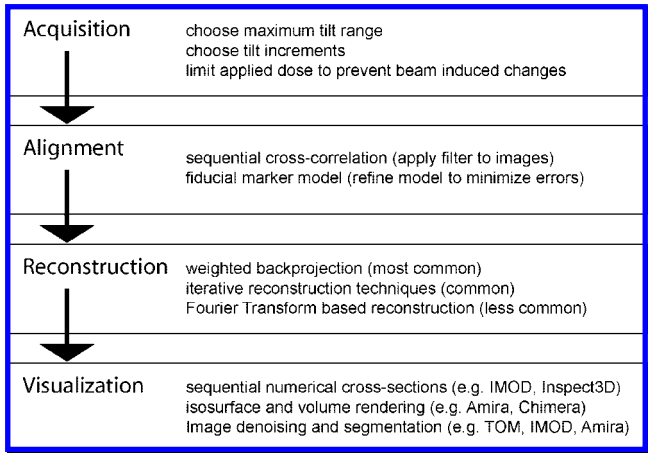

Figure 4. Workflow scheme.

The limiting factor for acquisition, in many cases, is electron-beam-induced damage to the specimen.[55,56] Care has to be taken that changes in the specimen are negligible and do not hamper the reconstruction. This does, however, not preclude ET from being applied to beam-sensitive materials such as frozen-hydrated (cryo) samples in life sciences. As pointed out by Hegerl and Hoppe in the dose-fractionation theorem, the electron dose required to detect structural features at a given level of statistical significance and resolution is the same for 2D and 3D imaging.[57] More recent computer simulations confirmed that the theorem is applicable to realistic experimental conditions.[58] For a more detailed discussion of Cryo-ET, we refer to the recent literature.[25,59]

To conclude the comments on acquisition, a cautioning remark on the amount of data that is acquired and will have to be processed seems appropriate. One tilt series recorded on a 2048 × 2048 pixel CCD camera over an angular range of ±70° at 1° increments will have a file size of approximately 1.1 GB (8 MB × 141 images).

While automated data collection is able to compensate for the major movements during acquisition, accurate alignment of the set of 2D images to a common origin and rotation axis has to be performed after data collection. Preceding alignment, TEM images are commonly corrected for pixels with unusually high values—"hot pixel"—that can be attributed to X-rays.[60] The two principal approaches to align a tilt series are alignment by cross-correlation[61] and alignment by tracking fiducial markers, i.e., colloidal gold.[53] In the case that the tilt-axis direction is known or can be determined, cross-correlation is a straightforward means for translational alignment. It is based on an overall match between image features common to two projections. To optimize results, appropriate numerical filters are employed to enhance image features that can be easily cross-correlated to each other and to reduce noise sensitivity.[21,61]

Alignment by tracking fiducial markers determines both translational alignment and the tilt-axis direction.[53] For a set of gold markers, commonly 10−30, a fiducial model is generated by tracking their centers either manually or by automated procedures throughout the entire image series. This model is then used to determine relative shifts and rotations between images, by applying least-squares minimization.[53] In general, fiducial models from automated tracking have to be refined. Finally, by applying the translational and rotational corrections, an aligned tilt series is obtained, from which the tomogram can be reconstructed.

Common academic and commercial software packages for alignment and reconstruction of ET data include IMOD,[62] TOM software toolbox,[40] EMMenu (TVIPS GmbH, Gauting, Germany), Inspect3D (FEI company, Eindhoven, The Netherlands), TEMography (JEOL Ltd., Tokyo, Japan), and Digital Micrograph 3D ET (Gatan Inc., Pleasanton, CA). Tomographic reconstruction is carried out using numerical algorithms of which weighted backprojection techniques (WBPs) are most common.[63] With increasing processing speed of desktop computers, iterative methods gain importance.[64−70] For a detailed discussion of reconstruction algorithms, we refer to the literature.[29,71]

The last step in the workflow is the visualization of 3D results. This is a rather broad topic, and approaches will differ depending on the structures under investigation or the imaging technique used. In general, the tomogram will contain intensity variations that are interpretable as variations in imaged object property, e.g., mass density. Common ways of presenting 3D data include the display of consecutive numerical cross sections as a movie, rendering of a surface belonging to a specific intensity value, and rendering of the

object volume with a color scheme where each color represents a certain range of intensities. While most of the above-mentioned alignment and reconstruction software packages include tools for visualization, often dedicated programs such as UCSF Chimera[72] and Amira (Mercury Computer Systems, Inc., Chelmsford, MA) are utilized.

Another very interesting and relevant approach, which provides quantitative structural information from ET data, is image analysis by segmentation.[73−75] Image segmentation is the process of dividing an image (here the tomogram) into its parts for further analysis. The type of analysis applied will differ depending on the scientific question but can include the particle-size distribution,[49,76] the particle location,[77,78] and the local curvature of surfaces,[56,79] of which examples will be given later in the article.

2.4. Imaging Modes

Electron microscopy provides a variety of modes to probe the sample, and as a result, there are a considerable number of possible ET modes, too. For a comprehensive overview, tested approaches are listed corresponding to the two most distinct modes for forming an image, i.e., parallel (TEM) or convergent (STEM) illumination, as outlined in Figure 1. For parallel illumination, bright-field (BF) ET,[32,33,49,78,80] annular dark-field (ADF) ET,[81] energy-filtered (EF) ET,[20,82−86] holographic ET,[87−89] weak-beam dark-field (WBDF) ET,[90] and diffraction ET[91,92] are reported in the literature. Using convergent illumination high-angle hollow-cone dark-field (HADF) ET,[93] annular dark-field (ADF) ET,[94,95] energy-dispersive X-ray (EDX) ET,[83] and high-angle annular dark-field (HAADF) ET[20,96] have been applied. In the following, we will restrict our discussion to BF TEM ET and HAADF STEM ET, since they are the most common techniques for studying catalysts. An example of EF TEM ET will be given in section 3.4.

For application to inorganic materials, care has to be taken that the images of the tilt series fulfill the projection requirement mentioned in section 2.1. A detailed assessment of the validity for BF TEM ET is given by Hawkes.[97] It is concluded that, for weakly scattering materials where mass thickness (absorption) is the dominant contrast mechanism, electron microscope images are essentially projections on which a tomographic reconstruction can be based. Alternatively, phase-contrast images are used for very weakly scattering objects, such as unstained life science specimens and polymers. However, in the case of crystalline materials, where Bragg diffraction significantly contributes to image formation, BF ET has been suggested to be of only limited value.[20,98] In contrast, many successful applications of BF ET to crystalline materials are reported in the literature.[99−102] The observation that orientation, i.e., diffraction condition, dependent contrast does not strongly effect the tomographic reconstruction can be rationalized by the fact that diffraction contrast is only present in a few images of the tilt series, while ET averages over a much larger number of images. An evaluation of the effect of Bragg diffraction on the reconstruction quality of BF TEM ET is given by Feng et al.,[103] and a direct comparison of TEM and STEM reconstructions of a crystalline object is given by Friedrich et al.[94] As a rule of thumb, crystalline domains should be small to prevent, e.g., thickness fringes and bend contours, and use of an objective aperture reduces the occurrence of displaced diffracted images and also the spatial resolution. In summary, it can be concluded that, for weakly scattering crystalline materials (zeolites) or highly scattering small crystallites (supported catalysts), BF TEM ET provides reliable 3D structural information.[47]

For 3D imaging of crystalline materials, predominantly incoherent signals, such as HAADF STEM and EF TEM, improve the projection relationship between mass density and image intensity.[20,83] HAADF STEM images (*Z*-contrast images) are formed by electrons scattered close to the nucleus of the atom. This causes the scattering cross section for *Z*-contrast to approach the unscreened Rutherford potential,[96] which is approximately proportional to the square of the atomic number Z.[2] To avoid effects from Bragg scattered electrons, the required inner collection angle of the detector can be estimated from the atomic thermal vibrations, which gives ∼40 mrad for silicon at 200 kV.[26,104] In addition, dynamical channeling effects may lead to changes in image intensity. The main advantage of HAADF STEM to be exceptionally sensitive to high-*Z* elements leads, on the other hand, to difficulties when imaging high and low-*Z* elements together. In HAADF STEM ET, optimized for reducing the Bragg effects of high-*Z* elements, low-*Z* elements are hard to detect, since they almost do not scatter electrons into large angles. For imaging of metal particles and carbon supports, combined approaches utilizing the bright-field and low-angle annular dark-field signals in addition to HAADF have been suggested.[95]

If one keeps the limitations of each technique in mind, in context with the composition and structure of the studied material as well as the scientific question, electron images are in first-approximation projections suitable for tomographic reconstruction. As a guide, low-*Z* materials containing small high-*Z* crystalline domains can be readily imaged in 3D by BF TEM and HAADF STEM ET. Furthermore, HAADF STEM ET increases the contrast for high-*Z* elements and reduces diffraction effects for large crystallites.

3. Applications

Applications of ET to catalyst materials are very broad, and the following sections are organized corresponding to the materials classes of zeolites, ordered mesoporous materials, disordered oxide supported catalysts, carbon materials, and miscellaneous materials.

3.1. Zeolites

Zeolites are crystalline microporous materials that are widely applied as catalysts in the chemical industry.[105] The first applications of ET to a zeolite system, and the first to heterogeneous catalysts in general, were published by Koster et al.[32,106] Characterization of an Ag/NaY crystal in 3D showed unequivocally the location of 10−40 nm Ag particles inside and outside the NaY structure. In addition, the first results on the viability of 3D imaging of mesopores in zeolites are given.[32] The special interest in imaging of mesopores can be concluded from recent reviews.[107,108] For applications like cracking of heavy oil fractions, cumene production, alkane hydroisomerization, and, more recently, fine chemicals synthesis, the shape and connectivity of mesopores in zeolite crystals is of major importance. The mesopores ensure an optimal accessibility and transport of reactants and products, while the zeolite micropores induce the preferred shape-selective properties.

ET has been used to study various strategies to introduce mesopores in zeolites, namely, steaming, acid leaching, base

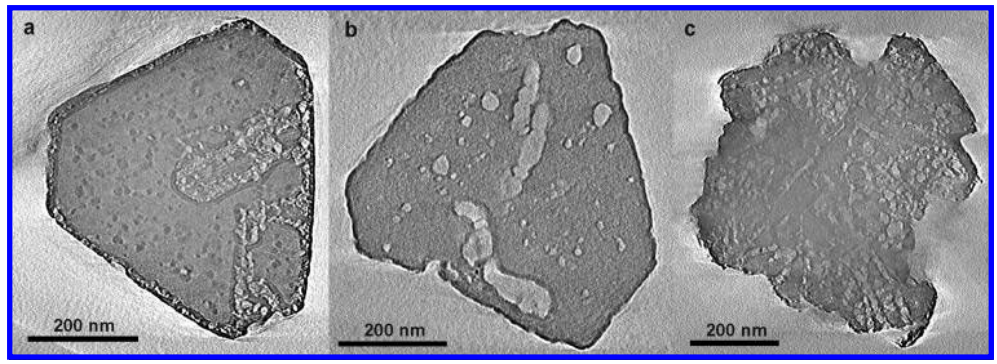

Figure 5. Slices through 3D reconstructions of steamed zeolite Y (a), steamed and acid-leached zeolite Y (b), and high-meso zeolite Y (c) showing the formation and connectivity of mesopores.

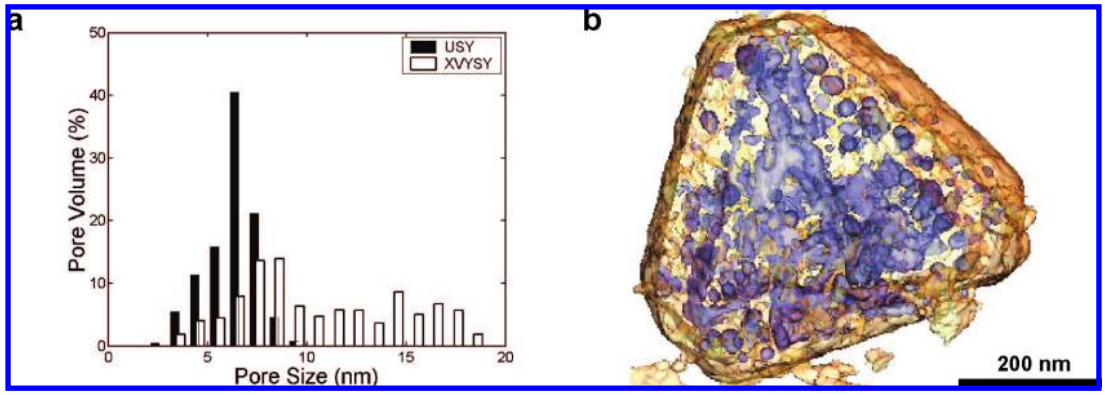

Figure 6. Mesopore size distributions of steamed zeolite Y (USY) and steamed and acid-leached zeolite Y (XVUSY) obtained by image analysis of electron tomograms (a) and 3D representation of steamed and acid-leached zeolite Y (b) showing the mesopores through the transparent surface of the particle.

leaching, and secondary templating during synthesis. Main objectives of these studies were to determine how the post- or pretreatments effect the three-dimensional location, shape, and connectivity of the mesopores. In two papers from our group, a detailed formation mechanism of mesopores was proposed by studying a series of steam-treated and acid-leached zeolite Y.[80,109] The tomograms in Figure 5 directly show that steaming and acid-leaching treatments are successful to obtain highly mesoporous zeolite Y crystals. It was concluded that mild treatments result in many cavities inside the crystals (parts a and b of Figure 5), while more severe treatments cause a loss of crystallinity and a decrease of micropore volume. After a special hydrothermal treatment (U.S. Patent 5601798 (PQ Corp)), zeolite Y crystals with very high mesopore volumes (Figure 5c) and networks consisting predominantly of interconnected cylindrical mesopores were obtained.

An alternative approach, first studied by Jacobsen et al., utilizes a secondary carbon template for creating intracrystalline mesopores during zeolite synthesis.[110] ET results showed that both carbon nanofibers and carbon black aggregates were capable to act as a template for cylindrical mesopores that start at the external surface of the zeolite crystals.[111] The tortuosity of the mesopores templated by the carbon black aggregates was much higher than the cylindrical mesopores templated by the carbon nanofibers.

The most recent approach introduces mesoporosity in zeolites by desilication, also referred to as base leaching.[112] In a study on the controlled desilication of ZSM-5, details of obtained 3D structures are reported.[113] While Al gradients lead to a rather uniform mesoporosity development in the interior of the crystal, the outer Al-rich surface remained relatively unaffected. Desilication coupled to ET is seen as a suitable tool to elucidate aluminum gradients, which in the future will enable the fabrication of highly porous particles with tunable void volumes, sizes, and accessibility.

As a last example, we would like to highlight the quantitative structural analysis of mesopores inside single zeolite crystals.[114] The results of the image analysis, displayed in Figure 6, confirm that quantization from ET is possible and agreed well with physisorption measurements of the bulk material.[109] While physisorption methods prevail in the characterization of the bulk mesopore properties, analysis of individual objects by ET does not assume a specific pore shape, which makes both approaches complementary.

The results presented in this section illustrate that bright-field TEM ET provides reliable 3D structural information of low-*Z* crystalline materials. Detailed insight into shape and connectivity of mesopores will contribute to enable a rational design of zeolite-based systems that display improved catalytic properties.

3.2. Ordered Mesoporous Materials

The introduction of ordered mesoporous materials (OMMs) has opened up a completely new field of research.[115,116] OMMs show great potential for applications ranging from chromatography, over drug delivery,[118] to catalysis.[119] OMM self-assembly is carried out by sol−gel synthesis in aqueous solution with various surfactants or polymer templates to allow a wide range of pore sizes, pore morphologies, and chemical compositions.

Structural elucidation of OMMs, commonly carried out by model-based analysis of electron micrographs, X-ray

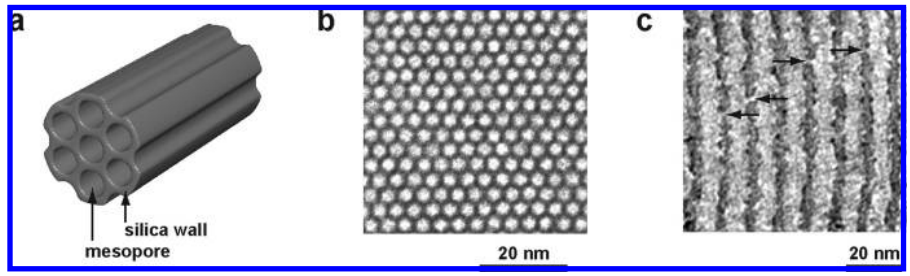

Figure 7. Model of 2D hexagonal pore ordering in MCM-41 and SBA-15 (a), TEM image of MCM-41 with a hexagonal pore shape (b), numerical cross section through reconstruction of SBA-15 showing corrugated mesopore walls in dark gray and pore connections by arrows (c).

diffraction (XRD), and physisorption data, can be aided by ET, in particular for complex nonrepeating morphologies that deviate from ideal geometry. To illustrate this point, in Figure 7 the pore structure of the two most prominent ordered mesoporous silicas (OMSs), namely, MCM-41 and SBA 15, are shown. While both OMSs expose a 2D hexagonal pore ordering[115,116] (Figure 7a), MCM-41 mesopores (Figure 7b) can have a hexagonal-to-round pore shape,[120,121] and SBA-15 mesopores (Figure 7c) are corrugated and interconnected.[122−124] In particular, the pore corrugation of SBA-15 requires a local description, which was recently provided by combining ET and image analysis.[125] Pore corrugation was modeled in terms of a locally variable pore radius and center, and results compared well with the corona model used to analyze XRD and physisorption data. Also, the mesoscopic ordering of SBA-15 pore has been examined by ET.[126] Although a 2D hexagonal lattice of mesopores existed on a microscopic scale, irregularly curved pores (U-shaped) on the mesoscopic length scale were also observed. Thus, the diffusion path length in curved pores may be much larger than commonly estimated from the particle size. A second example in this field revealed the local morphology of submicron Michigan State Univerity (MSU)-type particles.[127] It could be shown that the structure was composed of folded ribbons of hexagonally packed mesoporous silica, enclosing cavities inside the particle. The material (consisting of small particles, large pores, and cavities) was found to have very similar separation properties to those of commercial powders used in high-performance liquid chromatography. A detailed quantitative analysis of the 3D pore structure of chromatographic adsorbents can be found in the paper by Yao et al.[128]

More recent studies investigated macroporous ordered siliceous foams (MOSFs),[129] chiral mesoporous silica (CMS),[130] silica possessing a concentric circular mesostructure,[131] cage-type mesoporous silica FDU-12,[132] and periodic mesoporous organosilicas (PMOs).[133] The MOSFs form a honeycomb structure where each silica vesicle (∼100 nm diameter) is a hexagonal prism linked with three adjacent cells from the next layer.[129] For the CMS, prepared from achiral cationic surfactants, mesopores running spiral within the particle could be visualized. Particle morphology and the helical pitch could be systematically controlled by varying the ammonia concentration during preparation, and ET indicated that a particle can be composed of two helical rods of opposite handedness.[130] In contrast, silica with a concentric circular mesostructure was composed of hexagonally ordered pores without helical pitch, thus forming closed rings.[131] For the ordered cage-type mesoporous silica FDU-12, intergrowth between cubic and hexagonal close-packed structures was observed, and ET enabled the direct visualization of stacking faults.[132] Also in the PMO material, stacking faults could be visualized, but, most interestingly, changes in pore length and ordering could be tuned by the acidity of the reaction mixture.[133]

While the above examples utilized bright-field TEM ET, OMM materials can also be imaged using HAADF STEM ET as shown by the Midgley group. In an approach, referred to as real-space crystallography, the MCM-48 lattice structure was modeled.[134] ET results of the complex gyroid-like 3D pore network were consistent with the proposed space group of $Ia\bar{3}d$[135] but showed differences along the [111] zone axis. On the basis of the findings, a new pore model was suggested. Most notably, a grain boundary could be imaged in the MCM-48 particle, since ET resolves nonperiodic structures. This should not distract from the fact that electron crystallography of OMMs, pioneered by the Terasaki group, is an increasingly important technique in the field.[7,136,137]

For applications in catalysis, the ordered pore arrangement in combination with a very narrow pore-size distribution makes OMMs excellent model supports for active phases and reference systems to study catalyst preparation.[138] In particular for MCM-41, the first representative of ordered mesoporous silica (OMS), isomorphous substitution of metal ions into the silica framework or deposition of metal particles onto the mesopore surfaces have been extensively studied.[139] Not surprisingly, first applications of ET to this field dealt with MCM-41-supported metal particles. In a series of studies by the Midgley group, the dispersions of Pd_6Ru_6[20,96,140] and $Ru_{10}Pt_2$[141] in MCM-41 were studied. An account of the catalytic performance of bimetallic nanoparticles for hydrogenations is given by Thomas.[142] ET results of the Pd_6Ru_6 system proved that the mesoporous structure of the silica could be faithfully reconstructed with little sign of beam damage. The bimetallic particles did have a definite size distribution as a result of coalescence, with larger particles present outside the mesopores and the smaller ones present inside. For $Ru_{10}Pt_2$/MCM-41, a high particle density combined with good dispersion of the bimetallic phase inside the mesopores was observed (Figure 8).[141] Moreover, the local catalyst loading was calculated to be 1.4×10^{-5} g m^{-2} by counting the number of $Ru_{10}Pt_2$ particles and measuring the internal surface of the silica inside a subvolume of the reconstruction. From the fact that imaging of 12 atom clusters, known to be <1 nm in diameter, was successful, a tomographic resolution of ∼1 nm in all three dimensions could be inferred.[140,141] This value exceeds the resolution predicted by the Crowther criterion discussed in section 2.3.

Although MCM-41 has quite unique structural properties, its thin pore walls are prone to collapse in boiling water. In contrast, SBA-15 exhibits better hydrothermal stability as a result of its thicker silica walls.[116] Thus, SBA-15 can be applied over a larger range of reactions conditions and,

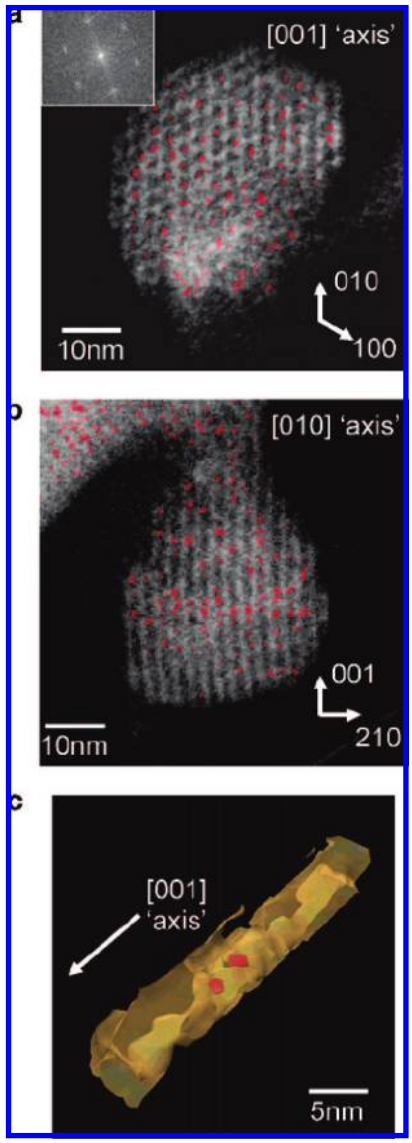

Figure 8. Two perpendicular voxel projections of MCM-41 supported Pt/Ru nanoparticles (a, b), and surface render of single mesopore segment with two nanoparticles inside (c). Reprinted with permission from ref 141. Copyright 2004 American Chemical Society.

therefore, is a suitable support material for heterogeneous catalysts. In a series of studies by our group, structural properties of SBA-15 model catalysts containing ZrO_2,[143] Au,[46,143] and NiO [49,144] particles were investigated. ET provided unequivocal information on the location and size of the metal (oxide) particles inside of the support. Microscopic observations, namely, blocking of mesopores by incorporated particles, could be directly correlated with features in the desorption isotherm of N_2-physisorption experiments.[143,144] For all guest phases (ZrO_2, Au, NiO), a nonuniform distribution of particles in the mesopores of the support was found. While in some pores many particles were present, other pores did not contain any particles.

The effect of an inhomogeneous distribution on the local loading in filled pores was studied in detail for NiO/SBA-15 model catalyst.[49] Quantification by image analysis showed that, locally, a loading twice the average bulk loading was present (Figure 9). The ET-derived NiO particle-size distribution was in agreement with the diameter obtained by XRD, and statistical analysis of the nearest-neighbor distances is only one possibility to utilize the information provided by ET for the study of catalysts. Additional examples for the quantitative analysis of electron tomograms are given by Ersen et al.[145]

The presented examples show that ET has become an indispensable technique for the 3D structural investigation of OMMs and OMM-based heterogeneous catalysts. It is also expected to facilitate understanding of OMS-templated nanostructures,[146] such as gold nanorods with tunable aspect ratios synthesized in SBA-15 by a seed-mediated growth.[147] Here, we also would like to mention applications of ET to nanostructures formed by alternative routes, such as Pt fibers grown by guided deposition of nanoparticles in a physically confined self-assembly of surfactants,[148] nanoporous gold fabricated by chemically dealloying AuAg films,[149] heterostructured GaP−GaAs nanowires grown by metal−organic vapor-phase epitaxy,[150] and helical or zigzagged GaN, $ZnGa_2O_4$, and Zn_2SnO_4 nanowires grown by the vapor−liquid−solid mechanism.[151]

3.3. Disordered Oxide Supported Catalysts

Disordered oxide-supported catalysts are often applied in industry since they combine a relatively high dispersion (amount of active surface) with a high degree of thermostability of the catalytically active component. In this section, silica and alumina supports are discussed, while other ceramics (ceria, zirconia, and titania) are presented in section 3.5. The first example in this section investigated the 3D localization of Pd particles in two Pd/SiO_2 cogelled catalysts.[76] Structural differences were quantified by image analysis, and an illustration of the results are presented in Figure 10. For a Pd loading of 1.1 wt %, an earlier simplified geometrical model could be confirmed, in which the Pd particles (4.4 ± 1.1 nm diameter) are located in the center of the primary silica particles (12.5 ± 4.8 nm diameter). When the Pd loading increased to 3.1 wt %, the diameter of the Pd particles increased slightly (4.8 ± 1.3 nm diameter), while the diameter of the silica skeleton decreased (10.3 ± 4.8 nm). ET proved that, for the higher loading, a significant fraction of the metal was also located outside the silica.

Alternatively to cogellation deposition of the active metal phase inside the silica, deposition of a catalyst precursor on the silica surface (i.e., by impregnation with a precursor-containing solution followed by drying and calcination) is also extensively used in catalyst preparation. In a case study by the Midgley group, ET was applied to image the dispersion in a highly effective Ru_5PtSn/SiO_2 catalyst for single-step hydrogenation.[152] The Ru_5PtSn phase had a tendency to be evenly distributed, mainly close to the surface of the silica particles, and no sintering occurred during exothermic hydrogenation. Further work of the same group focused on the dispersion of $Ru_8Pt_2C_2$ in silica gel combined ET with image analysis.[79] By determining the location of catalyst particles as a function of the local curvature of the support, as seen in Figure 11, preferential sites were classified. Nanoparticles within the interior preferred the saddle-shaped surfaces of the support, while nanoparticles at the support exterior were mainly located in saddlelike and cuplike regions. Such detailed 3D analysis of the metal particle location is key in improving the properties of hierarchically ordered systems.

Alternatively to silica, alumina is one of the most commonly used supports for preparation of, e.g., oil refining or Fischer−Tropsch (FT) catalysts. Two ET examples of oil

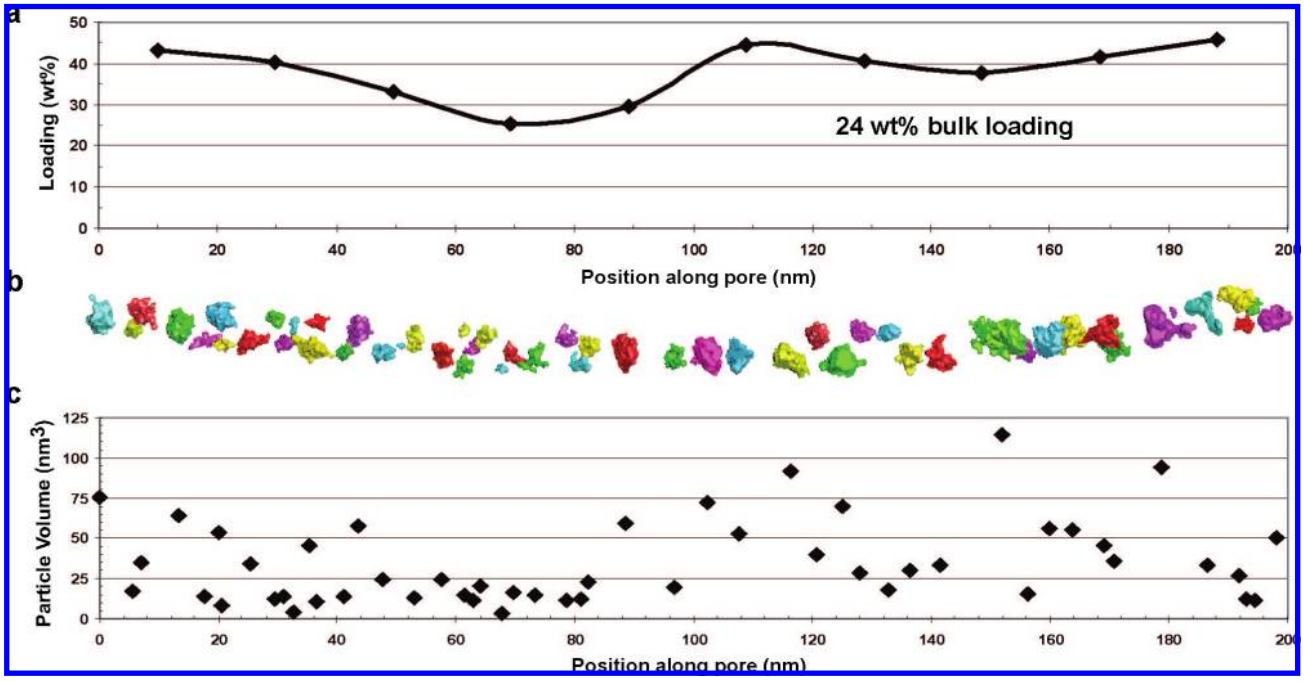

Figure 9. Local NiO loading in one SBA-15 mesopore (a), surface view of NiO crystallites in mesopore (b), and volume of crystallites plotted vs position along the mesopore (c). Reprinted with permission from ref 49. Copyright 2007 American Chemical Society.

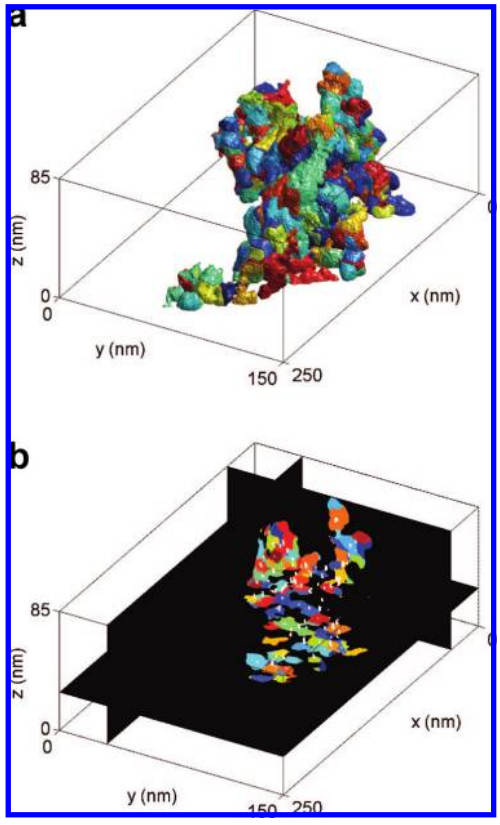

Figure 10. Quantitative analysis of 1.1 wt % Pd on SiO_2 cogelled catalyst by Voronoi tessellation of the silica skeleton. Each colored region corresponds to the silica shell around a specific Pd nanoparticle. Outer surface of the silica skeleton (a), and three numerical cross sections showing Pd particles in white (b). Reprinted with permission from ref 76. Copyright 2005 American Chemical Society.

refining catalysts are given by Kübel et al.[47] The studied catalysts were composed of a high surface area alumina support with well-dispersed small MoO_3 or Pt particles inside the structure. For the Pt-containing system, the resolution in

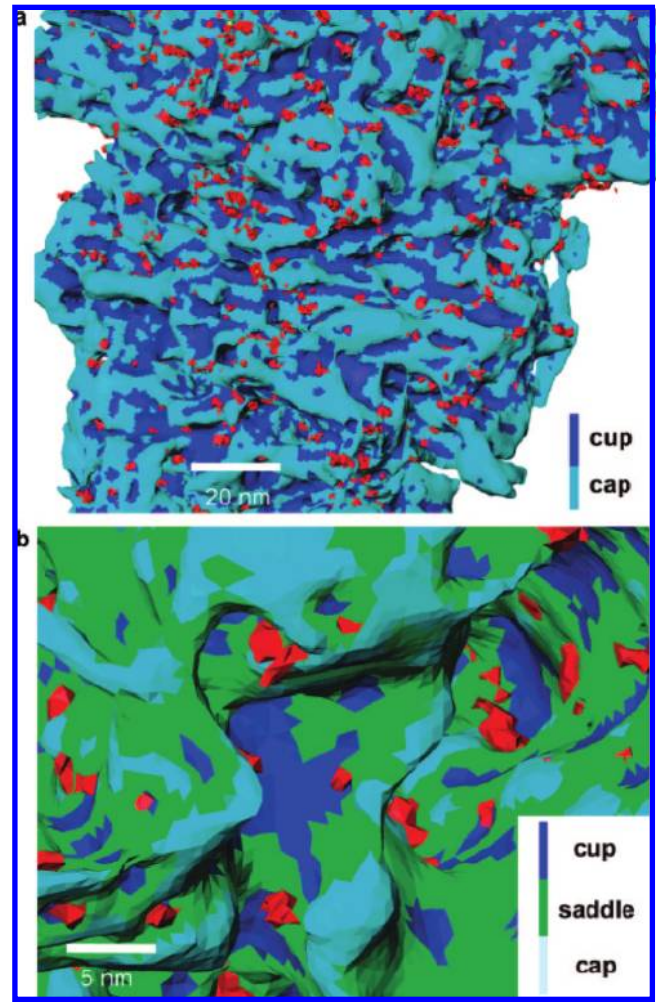

Figure 11. Region of the exterior silica surface colored according to its local curvature and Ru/Pt particles shown in red (a, b). The metal particles appear to be situated preferentially in positions with saddle to cuplike geometry. Reprinted with permission from ref 79. Copyright 2007 American Chemical Society.

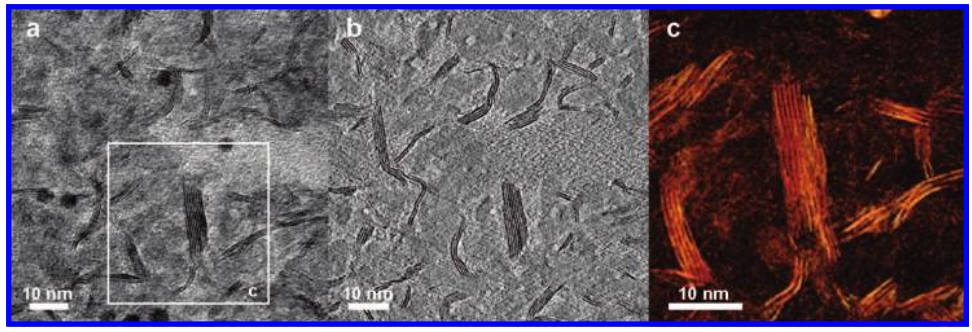

Figure 12. TEM image of a MoS_2/γ-Al_2O_3 catalyst with 5 nm gold particle (dark spots) attached to the thin section (a), slice through reconstruction showing the 0.6 nm spaced MoS_2 crystal planes (b), and voxel projection displaying only the complex interconnected MoS_2 network (c). Reprinted with permission from ref 153. Copyright 2006 American Chemical Society.

the reconstruction was sufficient to analyze the Pt particle-size distribution by means of line profiles. Pt particles had a diameter between 1 and 3 nm with a distribution maximum at ~1.8 nm. Further work by our group extended the use of ET to a commercial, sulfided Ni−Mo/γ-Al_2O_3 hydrotreating catalyst.[153] As seen in Figure 12, the MoS_2 particles in the pores of the support were imaged with sufficient accuracy to resolve the 0.6 nm spaced MoS_2 crystal planes. The MoS_2 particles form a complex interconnected structure within the mesopores, and their individual shape largely deviates from simple models as derived from studies on model catalysts. Without a doubt, such information is extremely valuable to aid in first-principle modeling of sulfide catalysts.[154] This includes recent strides toward atomic resolution tomography of MoS_2-based fullerene-like nanostructure by the combination of low-voltage electron microscopy with aberration-corrected phase-contrast imaging.[155]

The last example in this section deals with catalysts for the Fischer−Tropsch (FT) process that receive much attention in both academia and industry. In work by Arslan et al., the structure of two unreduced Re-promoted Co_3O_4/alumina FT catalysts was investigated.[156] It was concluded that the less C_{5+} selective catalyst consisted of fully interlocking metaloxide/γ-alumina aggregates. When a Ni impregnated and high-temperature heat-treated γ-alumina support is used, a fine distribution of Ni aluminate within a coarser α alumina skeleton is observed. In this catalyst the Co_3O_4 shows a preference to form nanocages around the Ni aluminate. After reduction, the metallic Co might display a more open local environment, which is believed to be responsible for the higher C_{5+} selectivity of this catalyst. The case studies cited in this section illustrate the potential of ET for investigating systems with a complexity approaching industrial catalysts at (sub)-nanometer resolution.

3.4. Carbon Materials

Carbon materials are widely used as catalyst supports, absorbents, and additives in the chemical, pharmaceutical, food, and agricultural industries because of their high surface area, low cost, and good chemical stability in liquid media. The most commonly used structures are activated carbons, carbon black, graphite, and carbon fibers/tubes. One of the advantages of carbon-based catalysts relates to the facile reclaim of noble metals simply by combusting the carbon. Since ET studies of nonfunctionalized carbon materials are sparse, existing examples will be given prior to the functionalized structures. At the end of this section, carbon nanotube/polymer composites and the morphology of carbon black emissions, in context with its environmental impact, will be discussed.

The first ET studies of carbon-based catalysts were carried out by the Midgley group using HAADF STEM ET on a Pd/C system.[67,157] The carbon support (400−600 nm in diameter) and the Pd nanoparticle aggregates larger than 6−10 nm could be successfully resolved in 3D. In some instances, clear clustering of the 1−20 nm sized particles was observed. Further work of the same group on a Pt/C system showed that, down to a size of 5 nm, the shape and size of the Pt particles was well-resolved.[158] However, characterization of the carbon matrix by HAADF STEM ET was difficult, and a combination with low-angle annular dark imaging was suggested to improve results (see also section 2.4).[95]

Two additional examples of ET to study the 3D structure of Pt/C catalysts are given by Wikander et al.[159] and Abrosimov et al.[48] In the former case ~3 nm sized Pt particles on an ordered mesoporous carbon (KIT 6 replica) were imaged, and in the latter, ~2−4 nm sized Pt particles on a poorly crystallized carbon support (Sibunit) were imaged. In both instances, ET confirmed that the particles were distributed at both the interior and exterior surfaces of the support and some larger agglomerates were present. For the Sibunit support (hollow carbon globules), BF TEM ET resolved a gap of 15 nm in the globule structure, rationalizing dispersion of the Pt particles in the inside.

Applications of Pd/C and Pt/C systems range from hydrogenations[160] to electrodes in fuel cells.[161] In a polymer electrolyte membrane (PEM)-type fuel cell, a polymer electrolyte (commonly Nafion) separates the two carbon electrodes. The Pd or Pt nanoparticulate catalyst is deposited inside the pores of the carbon. Therefore, efficient penetration of the pores by the polymer electrolyte, and hence effective electrical contact, is essential for the fuel cell performance. An ET study linked the performance of the PEM-type fuel cell to the Pt and the Nafion distribution.[162] It could be shown that an autoclave treatment promoted the penetration of the Nafion into carbon black pores smaller than 100 nm, where 90% of the Pt was located, thus improving utilization of the catalyst. Such detailed insight can also aid in evaluating the long-term stability of fuel cell systems.[163]

In context of mobile power sources, we also would like to mention ET results on carbon nanospheres (CNSs) used in Li-ion battery cathodes. An important strategy to improve the charge/discharge rate of the batteries is to interpenetrate the negative electrode and electrolyte on the nanoscale, thus increasing the effective interface area. An ET study showed that CNSs can have a heterogeneous core−shell structure.[164]

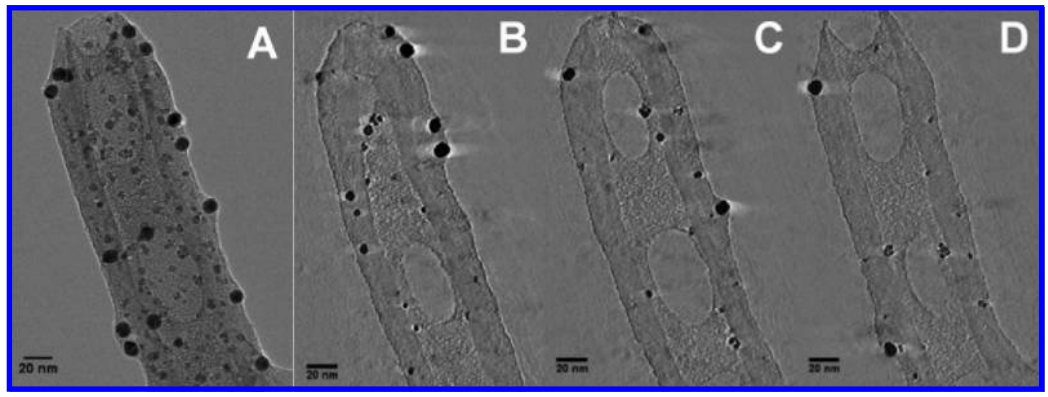

Figure 13. Palladium nanoparticles on the inside and outside of a multiwalled carbon nanotube. TEM image from the tilt series (A) and numerical cross sections through reconstruction (B−D). The presence of an amorphous phase (from suspension in ethanol for TEM sample preparation) wetting both the inside and the outside could be observed. The 10 nm sized spots on the outside are colloidal gold particles deposited to aid in alignment of the data set. Reprinted with permission from ref 78. Copyright 2007 American Chemical Society.

In combination with high-resolution TEM, it was concluded that the outside consisted of a series of ~10 nm thick faceted carbon walls, while the inside did not show graphitic ordering. Structure defects seemed to be concentrated along the ridgelines of the CNS particles and are possibly the ion paths causing improved battery performance. Application of ET to study the 3D structure of batteries has been suggested previously,[165] and now, with the first application showing success, a more extensive use can be expected.

Another carbon structure with great potential as catalyst support[166] are carbon nanotubes (CNTs).[167] In the first ET study of CNTs, the hollow core could be resolved in 3D, which until then was only inferred from 2D imaging.[168] In a recent paper by Bals et al., the morphology and composition of bamboolike CNTs including the catalyst particle were investigated.[169] ET results showed that the hollow compartments had a conelike 3D structure and that cavities were present in the catalyst particle. Intensity variations between different parts of the catalyst particle indicated an inhomogeneous composition, which was identified to be Cu and Cu_2O by EF TEM. Reconstruction of the 3D structure was carried out by an algorithm that combines reconstruction and segmentation, which allowed quantitative information on the individual phases to be obtained in a straightforward manner.

From an application point of view, interfaces between nanotubes and metals are of considerable interest. In work by the Muller group, the buried interfaces between nanotubes and the metal were studied by ET.[170] Samples were prepared by electron-beam evaporation of metals onto commercially purchased nanotubes. Gold was found to deform the nanotubes, creating flat contact surfaces. As one goes from poorly wetting gold to a gold−palladium alloy to palladium and finally to strongly wetting titanium, a decreasing tendency for nanotube deformation was observed.

Alternatively to outer surface functionalization, deposition of an active metallic phase inside CNTs could open up new possibilities in catalysis as a result of a synergetic confinement effect.[171] In this context, locating the position of the deposited particles with respect to the tube wall is crucial. In work by Ersen et al. the filling of multiwall CNTs by Pd particles (prepared from a nitrate precursor using aqueous impregnation) was investigated.[78] As seen in Figure 13, acid-treated tubes of 30 nm inner diameter had more than 50% of the Pd particles located on the inside. At 10 wt % loading, a homogeneous deposition on the inside of the multiwall (MW) CNT by 3−4 nm Pd particles with a density of 0.13 particles per nanometer tube length was derived. When decreasing the inner tube diameter to 15 nm, almost exclusive deposition on the outside was found. Interestingly, the diameter of the palladium particles was not affected by their location, i.e., inside or outside of the nanotube. Further work of the same author on $CoFe_2O_4$/CNTs related preparation effects (incipient wetness impregnation followed by calcination) to the average crystallite size and position in the CNT.[172] An example of the 3D morphology of a carbon-nanofiber-supported Fischer−Tropsch catalyst can be found in ref 173.

The next paragraph leaves catalysis-related applications and turns briefly to CNT/polymer composites. Despite their unique properties, research on CNTs is complicated by their strong cohesive nature, which limits dispersability. When wrapping single-wall CNTs with a water-soluble polymer, the dispersability increases, facilitating purification. Also from an application point of view, good dispersability is highly desired, since addition of a relatively small concentration of nanotubes to polymers significantly increases the electrical, thermal, and mechanical properties of the composite material. In a study on the wrapping of CNTs, it could be concluded that the polymer (in this case, polysaccharide) existed as a uniform layer around the CNTs.[174] An ET example on the incorporation of sodium dodecyl sulfate coated MWCNTs in a polystyrene matrix showed no CNT aggregation.[175] A potential problem when trying to image such composites is the similar contrast between the two carbon-based components. To enhance the contrast, EF TEM tomography can be employed.[85] Ratio images of the energy-filtered tomographic reconstructions clearly differentiate the MWCNT and the polymer (nylon) region. Low-loss spectra extracted from the bulk nylon, the nylon surface, a hole in the nylon, and the CNT hinted toward subtle differences in the corresponding electronic structure. One can envision further developments to obtain 3D information on the local bonding, which would be highly desired for catalytic applications. Additional studies utilizing EF TEM ET can be found in the references of section 2.4.

The end of this section dedicated to carbon materials deals with a topic of general interest closely related to catalysis, namely, air pollution generated from automotive engines. Despite the great improvements that fuel producers, car manufacturers, and legislation have made toward the abatement of pollution, certain limitations of combustion engines are hard to overcome. One important aspect is the incomplete combustion of fossil fuels, which in turn creates soot particles

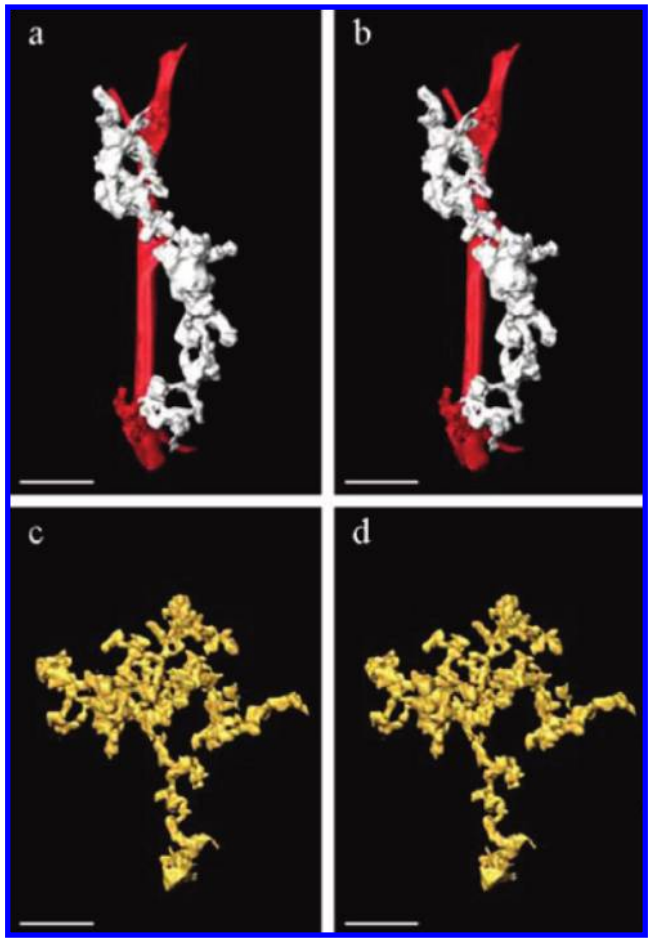

Figure 14. Stereo pairs (wide-eyed) of soot aggregates produced by incomplete combustion of biomass (a, b) and from a diesel engine (c, d), illustrating the complex fractal geometry of the structures. The vertical red bar in the top pair is the support for TEM imaging. Scale bars are 200 nm. Reproduced with permission from American Geophysical Union from ref 179. Copyright 2005 American Geophysical Union.

that are emitted in large quantities, ~8 Tg/year.[176] It was estimated that the overall contribution of soot to global warming may be second only to that of CO_2.[177,178] Soot typically aggregates into clusters (also referred to as mass fractals) that consist of numerous small primary particles. ET studies by the Buseck group investigated the 3D shapes of soot aggregates.[179,180] Two examples are displayed in Figure 14. It could be shown that morphological parameters (fractal dimension, radius of gyration, surface area) captured in 3D more accurately then 2D TEM values estimate atmospheric lifetimes utilized in global distribution models. Most importantly, the light-scattering properties of the complex aggregates were found to be up to 30 times larger than the values of unaggregated spheres commonly assumed to model the climate impact of soot.[180] In the future, such results are expected to be applied not only to improve climate models but also to minimize high-impact pollution.

3.5. Miscellaneous Materials

In this section, other materials like ceramics, polymers, and nanocomposites that have been investigated by ET are reviewed. While ceramic supports are often supposed to be inert (section 3.3), they can also expose catalytic properties.[181,182] Titanium dioxide in the anatase form, for example, is a photocatalyst under ultraviolet light (UV). A combined ET, in situ TEM, and electron energy loss spectroscopy (EELS) study observed structural changes from single-crystalline TiO_2 to polycrystals during photocatalytic oxidation of hydrocarbons.[183] When introducing extrinsic metals, UV-activated decomposition of organic and inorganic pollutants can be improved. To determine the 3D morphology of an Ag/TiO_2 catalyst manufactured by spray pyrolysis, ET was employed.[184] It could be shown that silver particles of <10 nm were uniformly dispersed on the inside and on the outside of the titania agglomerate. The spherical titania agglomerate, with a diameter of 150 nm, was composed of 10−20 nm titania particles.

Also, ceria and zirconia show properties that go beyond an inert support.[185,186] The application of ceria−zirconia mixed oxides to the three-way catalysts considerably reduced pollution by increasing the oxygen storage capacity and thermal stability of the system.[187] Enhanced redox properties can be induced by severe reduction followed by a mild oxidation.[188] This process has been associated with a transition from rounded crystallites to well-faceted oxide particles.[189] ET revealed a final particle shape very close to that of an octahedron. The observed change in morphology was also accompanied by an increase of Zr-rich, {111}-type surfaces, which could be key factors in understanding the distinct chemical behavior of the ceria−zirconia nanocrystals.[189] Further studies investigated the 3D structure of ceria nanocrystals in the context of their application as oxygen conductors in solid oxide fuel cells.[190] Crystals prepared by hydrothermal synthesis predominantly exposed {200} cubic facets, which offer the largest number of active sites. In combination with an average particle size of 6.7 nm, ensuring a high surface area, a high activity is expected.[190] To conclude the field of ceramics, we also would like to mention a recent materials science example in which ET was used to explore the morphology of ceria nanodendrites in an alkali−borosilcate glass matrix following a glass melting and annealing procedure.[191]

The next class of materials discussed in this section are polymers. Their main application in catalysis is as supports, e.g., for immobilization of homogeneous catalysts to improve catalyst recovery.[192,193] From a structural point of view, block copolymers, which self-organize into microphase-separated nanostructures, are of particular interest. ET studies of diblock copolymers show assembly into 3D structures composed of hexagonally stacked cylinders[194−196] and lamellar structures.[197−199] Triblock copolymers have been shown to form microdomain structures composed of cylinders with polygonal cross sections packed in square lattices[200] and in hexagonal lattices.[201] Porous supports can be obtained from the microphase-separated block copolymer by selective degradation of one of the microdomain phases.[202] A detailed 3D structural analysis of a porous polymer support containing Pd particles was carried out by Jinnai et al.[77] ET results unambiguously resolved the porous polymer network with most of the Pd particles located at the polymer/pore interface (Figure 15). Using image analysis, quantitative structural information such as the number of Pd particles per surface area (490 μm^{-2}), the Pd particle size distribution (~4.2 nm radius), and the penetration of the Pd particles into the surface (~1.2 nm) could be obtained. For a detailed account on the 3D structural characterization of polymers, we refer to a recent review.[55]

Closely related to many of the above materials is the field of nanocomposites, which was already discussed for carbon

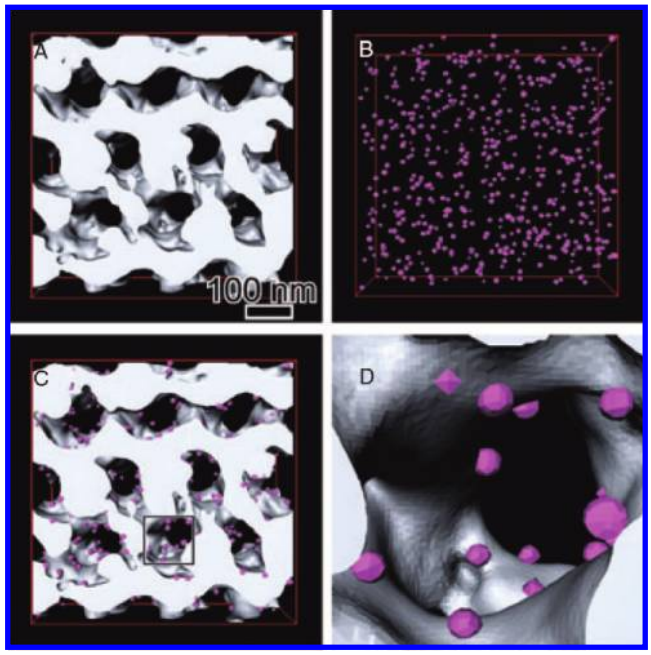

Figure 15. Surface visualization of porous polymer (A), Pd nanoparticles (B), superposition of porous polymer and Pd (C), and close-up view (D) of the region boxed in (C). Reprinted with permission from ref 77. Copyright 2006 John Wiley and Sons, Inc. and The Japan Chemical Forum.

nanotubes in section 3.4. Nanocomposites are created by introducing nanoparticulate fillers into a matrix material to tune electrical, thermal, and mechanical properties of the resulting system. Here we would like to mention ET studies on polymer nanocomposites containing silica,[203,204] carbon black,[204] carbon nanotubes,[85,175] and ceramics[205,206] as a few examples from the literature.

4. Conclusions and Outlook

The controlled assembly of functional materials on the nanoscale has been a major focus of research across many scientific disciplines over the last few decades.[115,116,167,207,208] These developments were in part fueled by the availability of characterization techniques, such as TEM, that can probe obtained structures with high spatial resolution. With the increasing complexity of nanomaterials and to gain precision in synthesis and assembly, elucidation of their full 3D morphology becomes more and more important.[33,209] Facilitated by automated ET data collection systems and high-performance desktop computing, ET is now used as a tool for the 3D structural characterization of inorganic materials.[20,32] At present, mainly bright-field TEM ET and high-angle annular dark-field STEM ET are applied, depending on sample composition, degree of crystallinity, and crystallite size. With the advent of aberration correctors for electron microscopy,[210,211] new opportunities for materials characterization arise,[212] potentially providing 3D information at atomic resolution.[17,155,213] In this review, we have given a number of examples that highlight the importance of ET in the field of catalysis. When studying hierarchical materials, such as mesoporous zeolites or supported catalysts, accurate knowledge of the 3D morphology significantly aids in understanding their physicochemical properties. To obtain unbiased quantitative structural information, image analysis can be considered as the next key step.[49,56,76,78,79,156] However, one cannot emphasize enough the linking of ET-derived results to bulk characterization techniques to ensure that statistically significant sample properties are described. Now the first examples using image segmentation (measuring porosity, particle-size distributions, or tortuosity) provide a microscopic explanation for bulk properties. With a wealth of nanostructural data at hand, the challenge ahead lies in relating this information to the catalytic properties of materials. ET delivers fundamental insights into the 3D structure of complex hierarchical materials and is expected to contribute significantly to rational catalyst design in the future.

5. Acknowledgments

H.F. and K.P.d.J. acknowledge financial support by the National Research School Combination Catalysis.

6. References

(1) Williams, D. B.; Carter, C. B. *Transmission electron microscopy: A textbook for materials science*; Springer Science + Business Media, Inc., A Division of Plenum Publishing Corporation: New York, 1996.
(2) Reimer, L. *Transmission Electron Microscopy*, 4th ed.; Springer-Verlag: Berlin, 1997.
(3) Yao, N., Wang, Z. L., Eds.; *Handbook of Microscopy for Nanotechnology*; Kluwer (now Springer): Boston, MA, 2005.
(4) Gai, P. L.; Boyes, E. D. *Electron Microscopy in Heterogeneous Catalysis*; Institute of Physics Publishing: Bristol, U.K., 2003.
(5) Thomas, J. M.; Terasaki, O. *Top. Catal.* **2002**, *21*, 155.
(6) Datye, A. K. *J. Catal.* **2003**, *216*, 144.
(7) Anderson, M. W.; Ohsuna, T.; Sakamoto, Y.; Liu, Z.; Carlsson, A.; Terasaki, O. *Chem. Commun.* **2004**, 907.
(8) Thomas, J. M.; Midgley, P. A. *Chem. Commun.* **2004**, 1253.
(9) Stroud, R. M.; Long, J. W.; Pietron, J. J.; Rolison, D. R. *J. Non-Cryst. Solids* **2004**, *350*, 277.
(10) Diaz, I.; Alfredsson, V.; Sakamoto, Y. *Curr. Opin. Colloid Interface Sci.* **2006**, *11*, 302.
(11) Gai, P. L. *Top. Catal.* **2002**, *21*, 161.
(12) Egerton, R. F. *Top. Catal.* **2002**, *21*, 185.
(13) Arbiol, J.; Rossinyol, E.; Cabot, A.; Peiro, F.; Cornet, A.; Morante, J. R.; Chen, F. L.; Liu, M. L. *Electrochem. Solid-State Lett.* **2004**, *7*, J17.
(14) Heinrichs, B.; Geus, J. W.; Lambert, S.; Pirard, J.-P. *J. Catal.* **2006**, *241*, 229.
(15) Li, F.; Wang, Z.; Ergang, N. S.; Fyfe, C. A.; Stein, A. *Langmuir* **2007**, *23*, 3996.
(16) Bovin, J. O.; Alfredsson, V.; Karlsson, G.; Carlsson, A.; Blum, Z.; Terasaki, O. *Ultramicroscopy* **1996**, *62*, 277.
(17) Borisevich, A. Y.; Lupini, A. R.; Pennycook, S. J. *Proc. Natl. Acad. Sci. U.S.A.* **2006**, *103*, 3044.
(18) Sakamoto, Y.; Kaneda, M.; Terasaki, O.; Zhao, D. Y.; Kim, J. M.; Stucky, G.; Shin, H. J.; Ryoo, R. *Nature* **2000**, *408*, 449.
(19) Dorset, D. L.; Roth, W. J.; Gilmore, C. J. *Acta Crystallogr., Sect. A* **2005**, *61*, 516.
(20) Midgley, P. A.; Weyland, M. *Ultramicroscopy* **2003**, *96*, 413.
(21) Midgley, P. A.; Weyland, M.; Stegmann, H. Applications of Electron Tomography. In *Advanced Tomographic Methods in Materials Research and Engineering*; Banhard, J., Ed.; Oxford University Press: Oxford, U.K., 2008; p 335.
(22) Koster, A. J.; Grimm, R.; Typke, D.; Hegerl, R.; Stoschek, A.; Walz, J.; Baumeister, W. *J. Struct. Biol.* **1997**, *120*, 276.
(23) Lucic, V.; Förster, F.; Baumeister, W. *Annu. Rev. Biochem.* **2005**, *74*, 833.
(24) McIntosh, R.; Nicastro, D.; Mastronarde, D. *Trends Cell Biol.* **2005**, *15*, 43.
(25) Koster, A. J.; Barcena, M. Cryotomography: Low-dose Automated Tomography of Frozen-Hydrated Specimens. In *Electron Tomography: Methods for Three-Dimensional Visualization of Structures in the Cell*; Frank, J., Ed.; Springer Science + Business Media, LLC: New York, 2006; p 113.
(26) Midgley, P. A.; Ward, E. P. W.; Hungria, A. B.; Thomas, J. M. *Chem. Soc. Rev.* **2007**, *36*, 1477.
(27) Möbus, G.; Inkson, B. J. *Mater. Today* **2007**, *10*, 18.
(28) Radon, J. *Ber. Sächs. Akad. Wiss. Leipzig, Math.-Phys. Kl.* **1917**, *69*, 262.
(29) Deans, S. R. *The Radon Transform and Some of Its Applications*; John Wiley & Sons, Inc.: New York, 1983; p vii.
(30) Hounsfield, G. N. *Science* **1980**, *210*, 22.
(31) Withers, P. J. *Mater. Today* **2007**, *10*, 26.

(32) Koster, A. J.; Ziese, U.; Verkleij, A. J.; Janssen, A. H.; de Jong, K. P. *J. Phys. Chem. B* **2000**, *104*, 9368.
(33) de Jong, K. P.; Koster, A. J. *ChemPhysChem* **2002**, *3*, 776.
(34) Hart, R. G. *Science* **1968**, *159*, 1464.
(35) Hoppe, W.; Langer, R.; Knesch, G.; Poppe, C. *Naturwissenschaften* **1968**, *55*, 333.
(36) de Rosier, D. J.; Klug, A. *Nature* **1968**, *217*, 130.
(37) Bonetta, L. *Nat. Methods* **2005**, *2*, 139.
(38) Zheng, Q. S.; Braunfeld, M. B.; Sedat, J. W.; Agard, D. A. *J. Struct. Biol.* **2004**, *147*, 91.
(39) Mastronarde, D. N. *J. Struct. Biol.* **2005**, *152*, 36.
(40) Nickell, S.; Forster, F.; Linaroudis, A.; Net, W. D.; Beck, F.; Hegerl, R.; Baumeister, W.; Plitzko, J. M. *J. Struct. Biol.* **2005**, *149*, 227.
(41) Radermacher, M. Ph.D. Thesis, Department of Physics, University of Munich, Munich, Germany, 1980.
(42) Penczek, P. A.; Marko, M.; Buttle, K.; Frank, J. *Ultramicroscopy* **1995**, *60*, 393.
(43) Mastronarde, D. N. *J. Struct. Biol.* **1997**, *120*, 343.
(44) Crowther, R. A.; de Rosier, D. J.; Klug, A. *Proc. R. Soc. London, Ser. A* **1970**, *317*, 310.
(45) Radermacher, M.; Hoppe, W. *Proc. 7th Eur. Congr. Electr. Micr.*, den Haag, The Netherlands, 1980; p 132.
(46) Ziese, U.; de Jong, K. P.; Koster, A. J. *Appl. Catal., A* **2004**, *260*, 71.
(47) Kübel, C.; Voigt, A.; Schoenmakers, R.; Otten, M.; Su, D.; Lee, T. C.; Carlsson, A.; Bradley, J. *Microsc. Microanal.* **2005**, *11*, 378.
(48) Abrosimov, O. G.; Moroz, E. M.; Chuvilin, A. L. *Kinet. Catal.* **2006**, *47*, 464.
(49) Friedrich, H.; Sietsma, J. R. A.; de Jongh, P. E.; Verkleij, A. J.; de Jong, K. P. *J. Am. Chem. Soc.* **2007**, *129*, 10249.
(50) Penczek, P. A. *J. Struct. Biol.* **2002**, *138*, 34.
(51) Unser, M.; Sorzano, C. O. S.; Thevenaz, P.; Jonic, S.; El-Bez, C.; De Carlo, S.; Conway, J. F.; Trus, B. L. *J. Struct. Biol.* **2005**, *149*, 243.
(52) Cardone, G.; Grunewald, K.; Steven, A. C. *J. Struct. Biol.* **2005**, *151*, 117.
(53) Lawrence, M. C. Least-Squares Method of Alignment using Markers. In *Electron Tomography: Three-Dimensional Imaging with the Transmission Electron Microscope*; Frank, J., Ed.; Plenum Press: New York, 1992; p 197.
(54) Ziese, U.; Janssen, A. H.; Murk, J. L.; Geerts, W. J. C.; Van der Krift, T.; Verkleij, A. J.; Koster, A. J. J. *Microsc. (Oxford)* **2002**, *205*, 187.
(55) Luther, P. K. Sample Shrinkage and Radiation Damage. In *Electron Tomography: Three-Dimensional Imaging with the Transmission Electron Microscope*; Frank, J., Ed.; Plenum Press: New York and London, 1992; p 39.
(56) Jinnai, H.; Nishikawa, Y.; Ikehara, T.; Nishi, T. *Adv. Polym. Sci.* **2004**, *170*, 115.
(57) Hegerl, R.; Hoppe, W. *Z. Naturforsch., A: Phys. Sci.* **1976**, *31*, 1717.
(58) McEwan, B. F.; Downing, K. H.; Glaeser, R. M. *Ultramicroscopy* **1995**, *60*, 357.
(59) Plitzko, J. M.; Baumeister, W. Cryoelectron Tomography (CET). In *Science of Microscopy*; Hawkes, P. W., Spence, J. C. H., Eds.; Springer Science + Business Media, LLC: New York, 2007; Vol. 1, p 535.
(60) Downing, K. H.; Hendrickson, F. M. *Ultramicroscopy* **1999**, *75*, 215.
(61) Frank, J.; McEwan, B. F. Alignment by Cross-Correlation. In *Electron Tomography: Three-Dimensional Imaging with the Transmission Electron Microscope*; Frank, J., Ed.; Plenum Press: New York, 1992; p 205.
(62) Kremer, J. R.; Mastronarde, D. N.; McIntosh, J. R. *J. Struct. Biol.* **1996**, *116*, 71.
(63) Radermacher, M. Weighted Back-Projection Methods. In *Electron Tomography: Three-Dimensional Imaging with the Transmission Electron Microscope*; Frank, J., Ed.; Plenum Press: New York, 1992; p 91.
(64) Gilbert, P. *J. Theor. Biol.* **1972**, *36*, 105.
(65) Gordon, R.; Bender, R.; Herman, G. T. *J. Theor. Biol.* **1970**, *29*, 471.
(66) Skoglund, U.; Ofverstedt, L.-G.; Burnett, R. M.; Bricogne, G. *J. Struct. Biol.* **1996**, *117*, 173.
(67) Weyland, M. *Top. Catal.* **2002**, *21*, 175.
(68) Batenburg, K. J. *Electr. Notes Discrete. Math.* **2005**, *20*, 247.
(69) Tong, J.; Arslan, I.; Midgley, P. A. *J. Struct. Biol.* **2006**, *153*, 55.
(70) Bilbao-Castro, J. R.; Merino, A.; Garcia, I.; Carazo, J. M.; Fernandez, J. J. *Parallel Comput.* **2007**, *33*, 250.
(71) Kuba, A.; Herman, G. T. Some Mathematical Concepts for Tomographic Reconstructions. In *Advanced Tomographic Methods in Materials Research and Engineering*; Banhard, J., Ed.; Oxford University Press: Oxford, U.K., 2008; p 19.
(72) Pettersen, E. F.; Goddard, T. D.; Huang, C. C.; Couch, G. S.; Greenblatt, D. M.; Meng, E. C.; Ferrin, T. E. *J. Comput. Chem.* **2004**, *25*, 1605.
(73) Ribeiro, E.; Shah, M. *Mach. Vision Appl.* **2006**, *17*, 147.
(74) Sandberg, K. *Method. Cell Biol.* **2007**, *79*, 769.
(75) Ohser, J.; Schladitz, K. Visualization, Processing and Analysis of Tomographic Data. In *Advanced Tomographic Methods in Materials Research and Engineering*; Banhard, J., Ed.; Oxford University Press: Oxford, U.K., 2008; p 37.
(76) Gommes, C. J.; de Jong, K.; Pirard, J. P.; Blacher, S. *Langmuir* **2005**, *21*, 12378.
(77) Jinnai, H.; Kaneko, T.; Nishioka, H.; Hasegawa, H.; Nishi, T. *Chem. Rec.* **2006**, *6*, 267.
(78) Ersen, O.; Werckmann, J.; Houlle, M.; Ledoux, M. J.; Pham-Huu, C. *Nano Lett.* **2007**, *7*, 1898.
(79) Ward, E. P. W.; Yates, T. J. V.; Fernandez, J. J.; Vaughan, D. E. W.; Midgley, P. A. *J. Phys. Chem. C* **2007**, *111*, 11501.
(80) Janssen, A. H.; Koster, A. J.; de Jong, K. P. *Angew. Chem., Int. Ed.* **2001**, *40*, 1102.
(81) Bals, S.; Van Tendeloo, G.; Kiesielowski, C. *Adv. Mater.* **2006**, *18*, 892.
(82) Möbus, G.; Inkson, B. J. *Appl. Phys. Lett.* **2001**, *79*, 1369.
(83) Möbus, G.; Doole, R. C.; Inkson, B. J. *Ultramicroscopy* **2003**, *96*, 433.
(84) Weyland, M.; Yates, T. J. V.; Dunin-Borkowski, R. E.; Laffont, L.; Midgley, P. A. *Scripta Mater.* **2006**, *55*, 29.
(85) Gass, M. H.; Koziol, K. K. K.; Windle, A. H.; Midgley, P. A. *Nano Lett.* **2006**, *6*, 376.
(86) Yurtsever, A.; Weyland, M.; Muller, D. A. *Appl. Phys. Lett.* **2006**, *89*, 151920.
(87) Lai, G.; Hirayama, T.; Ishizuka, K.; Tanji, T.; Tonomura, A. *Appl. Opt.* **1994**, *33*, 829.
(88) Lai, G.; Hirayama, T.; Fukuhara, A.; Ishizuka, K.; Tanji, T.; Tonomura, A. *J. Appl. Phys.* **1994**, *75*, 4593.
(89) Twitchett-Harrison, A. C.; Yates, T. J. V.; Newcomb, S. B.; Dunin-Borkowski, R. E.; Midgley, P. A. *Nano Lett.* **2007**, *7*, 2020.
(90) Barnard, J. S.; Sharp, J.; Tong, J.; Midgley, P. A. *Science* **2006**, *313*, 319.
(91) Kolb, U.; Gorelik, T.; Kübel, C.; Otten, M. T.; Hubert, D. *Ultramicroscopy* **2007**, *107*, 507.
(92) Kolb, U.; Gorelik, T.; Otten, M. T. *Ultramicroscopy* **2008**, *108*, 763.
(93) Kakibayashi, H.; Nakamura, K.; Tsuneta, R.; Mitsui, Y. *Jpn. J. Appl. Phys., Part 1* **1995**, *34*, 5032.
(94) Friedrich, H.; McCartney, M. R.; Buseck, P. R. *Ultramicroscopy* **2005**, *106*, 18.
(95) Cervera Gontard, L.; Dunin-Borkowski, R. E.; Chong, R. K. K.; Ozkaya, D.; Midgley, P. A. *J. Phys: Conf. Ser.* **2006**, *26*, 203.
(96) Weyland, M.; Midgley, P. A.; Thomas, J. M. *J. Phys. Chem. B* **2001**, *105*, 7882.
(97) Hawkes, P. W. The Electron Microscope as a Structure Projector. In *Electron Tomography: Three-Dimensional Imaging with the Transmission Electron Microscope*; Frank, J. E., Ed.; Plenum Press: New York, 1992; p 17.
(98) Thomas, J. M.; Midgley, P. A.; Yates, T. J. V.; Barnard, J. S.; Raja, R.; Arslan, I.; Weyland, M. *Angew. Chem., Int. Ed.* **2004**, *43*, 6745.
(99) Stegmann, H.; Engelmann, H. H.; Zschech, E. *Microelectron. Eng.* **2003**, *65*, 171.
(100) Kaneko, K.; Nagayama, R.; Inoke, K.; Noguchi, E.; Horita, Z. *Sci. Technol. Adv. Mater.* **2006**, *7*, 726.
(101) Park, J. B.; Lee, J. H.; Choi, H. R. *Appl. Phys. Lett.* **2007**, *90*, 093111.
(102) Zhang, H. B.; Zhang, X. L.; Wang, Y.; Takaoka, A. *Rev. Sci. Instrum.* **2007**, *78*, 013701.
(103) Feng, R.-J.; Watanabe, T.; Takaoka, A. *Proc. Int. Microsc. Conf. 16 (Sapporo, Japan)* **2006**, 698.
(104) Howie, A. *J. Microsc. (Oxford)* **1979**, *117*, 11.
(105) Corma, A. *Chem. Rev.* **1995**, *95*, 559.
(106) Koster, A. J.; Ziese, U.; Verkleij, A. J.; de Graaf, J.; Geus, J. W.; de Jong, K. P. *Stud. Surf. Sci. Catal.* **2000**, *130*, 329.
(107) van Donk, S.; Janssen, A. H.; Bitter, J. H.; de Jong, K. P. *Catal. Rev.—Sci. Eng.* **2003**, *45*, 297.
(108) Tao, Y. S.; Kanoh, H.; Abrams, L.; Kaneko, K. *Chem. Rev.* **2006**, *106*, 896.
(109) Janssen, A. H.; Koster, A. J.; de Jong, K. P. *J. Phys. Chem. B* **2002**, *106*, 11905.
(110) Jacobsen, C. J. H.; Madsen, C.; Houzvicka, J.; Schmidt, I.; Carlsson, A. *J. Am. Chem. Soc.* **2000**, *122*, 7116.
(111) Janssen, A. H.; Schmidt, I.; Jacobsen, C. J. H.; Koster, A. J.; de Jong, K. P. *Microporous Mesoporous Mater.* **2003**, *65*, 59.
(112) Ogura, M.; Shinomiya, S. Y.; Tateno, J.; Nara, Y.; Kikuchi, E.; Matsukata, H. *Chem. Lett.* **2000**, *29*, 882.
(113) Groen, J. C.; Bach, T.; Ziese, U.; Paulaime-van Donk, A. M.; de Jong, K. P.; Moulijn, J. A.; Perez-Ramirez, J. *J. Am. Chem. Soc.* **2005**, *127*, 10792.

(114) Ziese, U.; Gommes, C. J.; Blacher, S.; Janssen, A. H.; Koster, A. J.; de Jong, K. P. *Stud. Surf. Sci. Catal.* **2005**, *158*, 633.
(115) Kresge, C. T.; Leonowicz, M. E.; Roth, W. J.; Vartuli, J. C.; Beck, J. S. *Nature* **1992**, *359*, 710.
(116) Zhao, D. Y.; Feng, J. L.; Huo, Q. S.; Melosh, N.; Fredrickson, G. H.; Chmelka, B. F.; Stucky, G. D. *Science* **1998**, *279*, 548.
(117) Grün, M.; Kurganov, A. A.; Schacht, S.; Schüth, F.; Unger, K. K. *J. Chromatogr., A* **1996**, *740*, 1.
(118) Mal, N. K.; Fujiwara, M.; Tanaka, Y. *Nature* **2003**, *421*, 350.
(119) Corma, A. *Chem. Rev.* **1997**, *97*, 2373.
(120) Schacht, S.; Janicke, M.; Schüth, F. *Microporous Mesoporous Mater.* **1998**, *22*, 485.
(121) Muroyama, N.; Ohsuna, T.; Ryoo, R; Kubota, Y.; Terasaki, O. *J. Phys. Chem. C* **2006**, *110*, 10630.
(122) Kruk, M.; Jaroniec, M.; Ko, C. H.; Ryoo, R. *Chem. Mater.* **2000**, *12*, 1961.
(123) Ryoo, R.; Ko, C. H.; Kruk, M.; Antochshuk, V.; Jaroniec, M. *J. Phys. Chem. B* **2000**, *104*, 11465.
(124) Liu, Z.; Terasaki, O.; Ohsuna, T.; Hiraga, K.; Shin, H. J.; Ryoo, R. *ChemPhysChem* **2001**, *2*, 229.
(125) Gommes, C. J.; Friedrich, H.; Wolters, M.; de Jongh, P. E.; de Jong, K. P. *Chem. Mater.* 2009, accepted for publication.
(126) Janssen, A. H.; Van Der Voort, P.; Koster, A. J.; de Jong, K. P. *Chem. Commun.* **2002**, 1632.
(127) Martines, M. U.; Yeong, E.; Persin, M.; Larbot, A.; Voorhout, W. F.; Kübel, C. K. U.; Kooyman, P.; Prouzet, E. *C. R. Chim.* **2005**, *8*, 627.
(128) Yao, Y.; Czymmek, K. J.; Pazhianur, R.; Lenhoff, A. M. *Langmuir* **2006**, *22*, 11148.
(129) Wang, H.; Zhou, X.; Yu, M.; Wang, Y.; Han, L.; Zhang, J.; Yuan, P.; Auchterlonie, G.; Zou, J.; Yu, C. *J. Am. Chem. Soc.* **2006**, *128*, 15992.
(130) Han, Y.; Zhao, L.; Ying, J. Y. *Adv. Mater.* **2007**, *19*, 2454.
(131) Yuan, P.; Liu, N.; Zhao, L. Z.; Zhou, X. F.; Zhou, L.; Auchterlonie, G. J.; Yao, X. D.; Drennan, J.; Lu, G. Q.; Zou, J.; Yu, C. Z. *Angew. Chem., Int. Ed.* **2008**, *47*, 6670.
(132) Ersen, O.; Parmentier, J.; Solovyov, L. A.; Drillon, M.; Pham-Huu, C.; Werckmann, J.; Schultz, P. *J. Am. Chem. Soc.* **2008**, *130*, 16800.
(133) Vercaemst, C.; Friedrich, H.; de Jongh, P. E.; Neimark, A. V.; Goderis, B.; Verpoort, F.; van der Voort, P. *J. Phys. Chem. C* 2009, accepted for publication.
(134) Yates, T. J. V.; Thomas, J. M.; Fernandez, J. J.; Terasaki, O.; Ryoo, R.; Midgley, P. A. *Chem. Phys. Lett.* **2006**, *418*, 540.
(135) Sakamoto, Y.; Kim, T. W.; Ryoo, R.; Terasaki, O. *Angew. Chem., Int. Ed.* **2004**, *43*, 5231.
(136) Garcia-Bennett, A. E.; Che, S. N.; Miyasaka, K.; Sakamoto, Y.; Ohsuna, T.; Liu, Z.; Terasaki, O. *Stud. Surf. Sci. Catal.* **2005**, *156*, 11.
(137) Gao, C. B.; Sakamoto, Y.; Sakamoto, K.; Terasaki, O.; Che, S. N. *Angew. Chem., Int. Ed.* **2006**, *45*, 4295.
(138) Sietsma, J. R. A.; de Jongh, P. E.; van Dillen, A. J.; de Jong, K. P. *Stud. Surf. Sci. Catal.* **2006**, *162*, 95.
(139) Ciesla, U.; Schüth, F. *Microporous Mesoporous Mater.* **1999**, *27*, 131.
(140) Midgley, P. A.; Weyland, M.; Thomas, J. M.; Johnson, B. F. G. *Chem. Commun.* 2001, 907.
(141) Midgley, P. A.; Thomas, J. M.; Laffont, L.; Weyland, M.; Raja, R.; Johnson, B. F. G.; Khimyak, T. *J. Phys. Chem. B* **2004**, *108*, 4590.
(142) Thomas, J. M.; Raja, R.; Johnson, B. F. G.; Hermans, S.; Jones, M. D.; Khimyak, T. *Ind. Eng. Chem. Res.* **2003**, *42*, 1563.
(143) Janssen, A. H.; Yang, C. M.; Wang, Y.; Schuth, F.; Koster, A. J.; de Jong, K. P. *J. Phys. Chem. B* **2003**, *107*, 10552.
(144) Sietsma, J. R. A.; Friedrich, H.; Broersma, A.; Versluijs-Helder, M.; van Dillen, A. J.; de Jongh, P. E.; de Jong, K. P. *J. Catal.* **2008**, *260*, 227.
(145) Ersen, O.; Hirlimann, C.; Drillon, A.; Werckmann, J.; Tihay, F.; Pham-Huu, C.; Crucifix, C.; Schultz, P. *Solid State Sci.* **2007**, *9*, 1088.
(146) Thiruvengadathan, R.; Levi-Kalisman, Y.; Regev, O. *Curr. Opin. Colloid Interface Sci.* **2005**, *10*, 280.
(147) Li, Z.; Kübel, C.; Parvulescu, V. I.; Richards, R. *ACS Nano* **2008**, *2*, 1205.
(148) Yamauchi, Y.; Takai, A.; Nagaura, T.; Inoue, S.; Kuroda, K. *J. Am. Chem. Soc.* **2008**, *130*, 5426.
(149) Fujita, T.; Qian, L. H.; Inoke, K.; Erlebacher, J.; Chen, M. W. *Appl. Phys. Lett.* **2008**, *92*, 251902.
(150) Verheijen, M. A.; Algra, R. E.; Borgström, M. T.; Immink, G.; Sourty, E.; van Enckevort, W. J. P.; Vlieg, E.; Bakkers, E. P. A. M. *Nano Lett.* **2007**, *7*, 3051.
(151) Kim, H. S.; Hwang, S. O.; Myung, Y.; Park, J.; Bae, S. Y.; Ahn, J. P. *Nano Lett.* **2008**, *8*, 551.
(152) Hungria, A. B.; Raja, R.; Adams, R. D.; Captain, B.; Thomas, J. M.; Midgley, P. A.; Golovko, V.; Johnson, B. F. G. *Angew. Chem., Int. Ed.* **2006**, *45*, 4782.
(153) de Jong, K. P.; van den Oetelaar, L. C. A.; Vogt, E. T. C.; Eijsbouts, S.; Koster, A. J.; Friedrich, H.; de Jongh, P. E. *J. Phys. Chem. B* **2006**, *110*, 10209.
(154) Raybaud, P. *Appl. Catal., A* **2007**, *322*, 76.
(155) Bar Sadan, M.; Houben, L.; Wolf, S. G.; Enyashin, A.; Seifert, G.; Tenne, R.; Urban, K. *Nano Lett.* **2008**, *8*, 891.
(156) Arslan, L.; Walmsley, J. C.; Rytter, E.; Bergene, E.; Midgley, P. A. *J. Am. Chem. Soc.* **2008**, *130*, 5716.
(157) Midgley, P. A.; Weyland, M.; Thomas, J. M.; Gai, P. L.; Boyes, E. D. *Angew. Chem., Int. Ed.* **2002**, *41*, 3804.
(158) Cervera Gontard, L.; Dunin-Borkowski, R. E.; Ozkaya, D.; Hyde, T.; Midgley, P. A.; Ash, P. *J. Phys: Conf. Ser.* **2006**, *26*, 367.
(159) Wikander, K.; Hungria, A. B.; Midgley, P. A.; Palmqvist, A. E. C.; Holmberg, K.; Thomas, J. M. *J. Colloid Interface Sci.* **2007**, *305*, 204.
(160) Gallezot, P.; Richard, D. *Cat. Rev.—Sci. Eng.* **1998**, *40*, 81.
(161) Liu, Z. L.; Hong, L.; Tham, M. P.; Lim, T. H.; Jiang, H. X. *J. Power Sources* **2006**, *161*, 831.
(162) Uchida, H.; Song, J. M.; Suzuki, S.; Nakazawa, E.; Baba, N.; Watanabe, M. *J. Phys. Chem. B* **2006**, *110*, 13319.
(163) Drennan, J.; Webb, R.; Nogita, K.; Knibbe, R.; Auchterlonie, G.; Tatenuma, K.; Hunter, J. *Solid State Ionics* **2006**, *177*, 1649.
(164) Yoshizawa, N.; Tanaike, O.; Hatori, H.; Yoshikawa, K.; Kondo, A.; Abe, T. *Carbon* **2006**, *44*, 2558.
(165) Long, J. W.; Dunn, B.; Rolison, D. R.; White, H. S. *Chem. Rev.* **2004**, *104*, 4463.
(166) Ebbesen, T. W. Properties: Experimental Results. In *Carbon Nanotubes, Preparation and Properties*; Ebbesen, T. W., Ed.; CRC Press: New York, 1997; p 225.
(167) Iijima, S. *Nature* **1991**, *354*, 56.
(168) Kizuka, T.; Sumi, T.; Bansho, S.; Saito, T. *Jpn. J. Appl. Phys., Part 2* **2001**, *40*, L56.
(169) Bals, S.; Batenburg, K. J.; Verbeeck, J.; Sijbers, J.; Van Tendeloo, G. *Nano Lett.* **2007**, *7*, 3669.
(170) Cha, J. J.; Weyland, M.; Briere, J. F.; Daykov, I. P.; Arias, T. A.; Muller, D. A. *Nano Lett.* **2007**, *7*, 3770.
(171) Pan, X. L.; Fan, Z. L.; Chen, W.; Ding, Y. J.; Luo, H. Y.; Bao, X. H. *Nat. Mater.* **2007**, *6*, 507.
(172) Ersen, O.; Begin, S.; Houlle, M.; Amadou, J.; Janowska, I.; Greneche, J.-M.; Crucifix, C.; Pham-Huu, C. *Nano Lett.* **2008**, *8*, 1033.
(173) Jacoby, M. *Chem. Eng. News* **2008**, *86*, 31.
(174) Numata, M.; Asai, M.; Kaneko, K.; Bae, A. H.; Hasegawa, T.; Sakurai, K.; Shinkai, S. *J. Am. Chem. Soc.* **2005**, *127*, 5875.
(175) Yu, J. R.; Lu, K. B.; Sourty, E.; Grossiord, N.; Konine, C. E.; Loos, J. C. *Carbon* **2007**, *45*, 2897.
(176) Bond, T. C.; Streets, D. G.; Yarber, K. F.; Nelson, S. M.; Woo, J. H.; Klimont, Z. *J. Geophys. Res.* **2004**, *109*, D14203.
(177) Hansen, J.; Sato, M.; Ruedy, R.; Lacis, A.; Oinas, V. *Proc. Natl. Acad. Sci. U.S.A.* **2000**, *97*, 9875.
(178) Jacobson, M. Z. *J. Geophys. Res.* **2001**, *106*, 1551.
(179) van Poppel, L. H.; Friedrich, H.; Spinsby, J.; Chung, S. H.; Seinfeld, J. H.; Buseck, P. R. *Geophys. Res. Lett.* **2005**, *32*, L24811.
(180) Adachi, K.; Chung, S. H.; Friedrich, H.; Buseck, P. R. *J. Geophys. Res.* **2007**, *112*, D14202.
(181) Coronas, J.; Santamaria, J. *Catal. Today* **1999**, *51*, 377.
(182) Keane, M. A. *J. Mater. Sci.* **2003**, *38*, 4661.
(183) Yoshida, K.; Nanbara, T.; Yamasaki, J.; Tanaka, N. *J. Appl. Phys.* **2006**, *99*, 084908.
(184) Kaneko, K.; Nagayama, R.; Inoke, K.; Noguchi, E.; Horita, Z. *Sci. Technol. Adv. Mater.* **2006**, *7*, 726.
(185) Reddy, B. M.; Thrimurthulu, G.; Saikia, P.; Bharali, P. *J. Mol. Catal., A: Chem.* **2007**, *275*, 167.
(186) Simonsen, S. B.; Dahl, S.; Johnson, E.; Helveg, S. *J. Catal.* **2008**, *255*, 1.
(187) Kaspar, J.; Fornasiero, P.; Hickey, N. *Catal. Today* **2003**, *77*, 419.
(188) Fornasiero, P.; Montini, T.; Graziani, M.; Kaspar, J.; Hungria, A. B.; Martinez-Arias, A.; Conesa, J. C. *Phys. Chem. Chem. Phys.* **2002**, *4*, 149.
(189) Hernandez, J. C.; Hungria, A. B.; Perez-Omil, J. A.; Trasobares, S.; Bernal, S.; Midgley, P. A.; Alavi, A.; Calvino, J. J. *J. Phys. Chem. C* **2007**, *111*, 9001.
(190) Kaneko, K.; Inoke, K.; Freitag, B.; Hungria, A. B.; Midgley, P. A.; Hansen, T. W.; Zhang, J.; Ohara, S.; Adschiri, T. *Nano Lett.* **2007**, *7*, 421.
(191) Xu, X.; Saghi, Z.; Yang, G.; Hand, R. J.; Möbus, G. *Cryst. Growth Des.* **2008**, *8*, 1102.
(192) Bergbreiter, D. E. *Curr. Opin. Drug Discovery Dev.* **2001**, *4*, 736.
(193) van de Coevering, R.; Gebbink, R. J. M. K.; van Koten, G. *Prog. Polym. Sci.* **2005**, *30*, 474.
(194) Spontak, R. J.; Williams, M. C.; Agard, D. A. *Polymer* **1988**, *29*, 387.
(195) Radzilowski, L. H.; Carragher, B. O.; Stupp, S. I. *Macromolecules* **1997**, *30*, 2110.

(196) Sugimori, H.; Nishi, T.; Jinnai, H. *Macromolecules* **2005**, *38*, 10226.
(197) Spontak, R. J.; Fung, J. C.; Braunfeld, M. B.; Sedat, J. W.; Agard, D. A.; Ashraf, A.; Smith, S. D. *Macromolecules* **1996**, *29*, 2850.
(198) Ikehara, T.; Jinnai, H.; Kaneko, T.; Nishioka, H.; Nishi, T. *J. Polym. Sci., Part B: Polym. Phys.* **2007**, *45*, 1122.
(199) Kato, M.; Ito, T.; Aoyama, Y.; Sawa, K.; Kaneko, T.; Kawase, N.; Jinnai, H. *J. Polym. Sci., Part B: Polym. Phys.* **2007**, *45*, 677.
(200) Yamauchi, K.; Takahashi, K.; Hasegawa, H.; Iatrou, H.; Hadjichristidis, N.; Kaneko, T.; Nishikawa, Y.; Jinnai, H.; Matsui, T.; Nishioka, H.; Shimizu, M.; Furukawa, H. *Macromolecules* **2003**, *36*, 6962.
(201) Takano, A.; Wada, S.; Sato, S.; Araki, T.; Hirahara, K.; Kazama, T.; Kawahara, S.; Isono, Y.; Ohno, A.; Tanaka, N.; Matsushita, Y. *Macromolecules* **2004**, *37*, 9941.
(202) Hashimoto, T.; Tsutsumi, K.; Funaki, Y. *Langmuir* **1997**, *13*, 6869.
(203) Schneider, G. J.; Fink, S. A.; Rachel, R.; Goritz, D. *Kautsch. Gummi Kunstst.* **2005**, *58*, 461.
(204) Jinnai, H.; Shinbori, Y.; Kitaoka, T.; Akutagawa, K.; Mashita, N.; Nishi, T. *Macromolecules* **2007**, *40*, 6758.
(205) Nishioka, H.; Niihara, K. I.; Kaneko, T.; Yamanaka, J.; Inoue, T.; Nishi, T.; Jinnai, H. *Compos. Interface* **2006**, *13*, 589.
(206) Kawase, N.; Kato, M.; Nishioka, H.; Jinnai, H. *Ultramicroscopy* **2007**, *107*, 8.
(207) Treacy, M. M. J.; Newsam, J. M. *Nature* **1988**, *332*, 249.
(208) Lin, Y.; Boker, A.; He, J. B.; Sill, K.; Xiang, H. Q.; Abetz, C.; Li, X. F.; Wang, J.; Emrick, T.; Long, S.; Wang, Q.; Balazs, A.; Russell, T. P. *Nature* **2005**, *434*, 55.
(209) Arslan, I.; Yates, T. J. V.; Browning, N. D.; Midgley, P. A. *Science* **2005**, *309*, 2195.
(210) Haider, M.; Uhlemann, S.; Schwan, E.; Rose, H.; Kabius, B.; Urban, K. *Nature* **1998**, *392*, 768.
(211) Krivanek, O. L.; Dellby, N.; Lupini, A. R. *Ultramicroscopy* **1999**, *78*, 1.
(212) Smith, D. J. *Microsc. Microanal.* **2008**, *14*, 2.
(213) Jinschek, J. R.; Batenburg, K. J.; Calderon, H. A.; Kilaas, R.; Radmilovic, V.; Kisielowski, C. *Ultramicroscopy* **2008**, *108*, 589.

CR800434T